



Cite as

Nano-Micro Lett.  
(2022) 14:100

## Next-Generation Intelligent MXene-Based Electrochemical Aptasensors for Point-of-Care Cancer Diagnostics

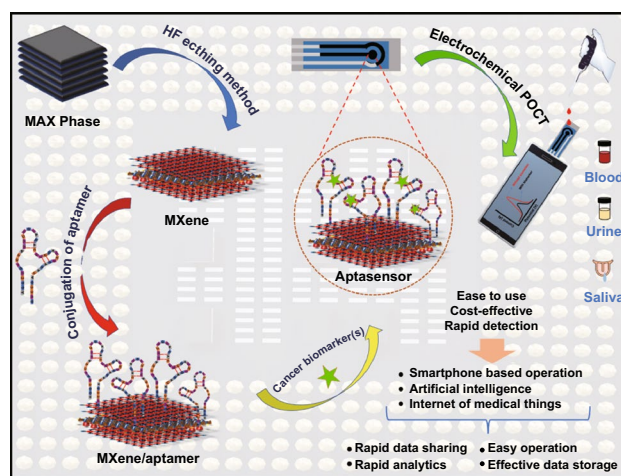
Arpana Parihar<sup>1</sup>, Ayushi Singhal<sup>1,2</sup>, Neeraj Kumar<sup>1,2</sup>, Raju Khan<sup>1,2</sup> ✉,  
Mohd. Akram Khan<sup>1</sup>, Avanish K. Srivastava<sup>1,2</sup>

Received: 22 January 2022  
Accepted: 11 March 2022  
© The Author(s) 2022

### HIGHLIGHTS

- Shed light on MXene-based electrochemical aptasensors for the detection of cancer biomarkers.
- Strategies for the design and synthesis of biomarker-specific aptamer are presented.
- The properties such as electrical conductivity, chemical stability, mechanical properties, and the hydrophilic–hydrophobic nature of MXenes are discussed.
- Brief insight on futuristic sensing applications along with challenges are highlighted.

**ABSTRACT** Delayed diagnosis of cancer using conventional diagnostic modalities needs to be addressed to reduce the mortality rate of cancer. Recently, 2D nanomaterial-enabled advanced biosensors have shown potential towards the early diagnosis of cancer. The high surface area, surface functional groups availability, and excellent electrical conductivity of MXene make it the 2D material of choice for the fabrication of advanced electrochemical biosensors for disease diagnostics. MXene-enabled electrochemical aptasensors have shown great promise for the detection of cancer biomarkers with a femtomolar limit of detection. Additionally, the stability, ease of synthesis, good reproducibility, and high specificity offered by MXene-enabled aptasensors hold promise to be the mainstream diagnostic approach. In this review, the design and fabrication of MXene-based electrochemical aptasensors for the detection of cancer biomarkers have been discussed. Besides, various synthetic processes and useful properties of MXenes which can be tuned and optimized easily and efficiently to fabricate sensitive biosensors have been elucidated. Further, futuristic sensing applications along with challenges will be deliberated herein.



**KEYWORDS** MXene; Electrochemical devices; POCT; Aptamer; Cancer diagnostics

✉ Raju Khan, [khan.raju@gmail.com](mailto:khan.raju@gmail.com); [khan.raju@ampri.res.in](mailto:khan.raju@ampri.res.in)

<sup>1</sup> Industrial Waste Utilization, Nano and Biomaterials, CSIR-Advanced Materials and Processes Research Institute (AMPRI), Hoshangabad Road, Bhopal 462026, MP, India

<sup>2</sup> Academy of Scientific and Innovative Research (AcSIR), Ghaziabad 201002, India

## 1 Introduction

Cancer is one of the major threats to the life and leading cause of death. As per the WHO estimations, cancer is the first or second leading cause of death for people aged below 70 in 112 countries out of the 183 countries and is the third or fourth leading cause in 23 other countries [1]. As per the estimation provided by The International Agency for Research on Cancer (IARC), during the lifetime of a person 1 in 5 people develops cancer. One woman out of 11 women dies with cancer, whereas 1 out of 8 men dies. About 50 million people are living with 5-year history of cancer. Breast, colorectal, lung, cervical, and thyroid cancers are common cancers among women. Lung and prostate cancer are common cancer in men. It was predicted in GLOBOCAN 2020 report that the countries which are identified as low or medium human development index would have the most increase in cancer cases by 2040 [2]. The estimated number of incident cases and mortality associated with various types of cancer is represented in the bar graph in Fig. 1a. The increasing rate of cancer incidence can be controlled if diagnosed at an early stage. Diagnosis at an early stage is quite a difficult challenge because cancer can be asymptomatic which can mislead the diagnosis [3]. Cancer progression is associated with different types of biomarkers. For instance, EGFR, VEGF, HER2, EpCAM, Mucin 1, CEA, CD44 are some important biomarkers found to be associated with the development and progression of cancer [4]. The quantification of these biomarkers can state the stage of cancer progression [5, 6]. By exploring the new technologies and strategies, diseases can be detected at an early stage and can decrease the death rate, and can save lives [7]. Biomarker's study can be benefited in multiple ways such as risk assessment [8], diagnosis [9], prognosis [10], predicting the treatment efficiency [11], toxicity [12], recurrence of any type of tumor, and many more [13]. The identification of biomarkers associated with a specific type of cancer can help to develop reliable and cost-effective diagnostics to detect cancer at an early stage and monitor it throughout the process of treatment [6, 14, 15]. For cancer diagnosis, conventional techniques such as PET, CT, X-ray, mammography, and tissue biopsy are the mainstream diagnostic modality being still used. However, these techniques failed to detect cancer at an early stage and need a centralized laboratory facility along with trained personnel. Besides, these conventional techniques, molecular techniques such as polymerase

chain reaction (PCR), enzyme-linked immunosorbent assay (ELISA), electrophoresis are also used; however, these methods lack accuracy, sensitivity, and selectivity [16].

Recently, biosensors-based advanced diagnostic approaches have shown potential for the early diagnosis of cancer and other deadly diseases [6, 16, 17]. Several techniques employed for the detections are optical [18, 19], electrochemical [20, 21], and piezoelectric [22]. The electrochemical-based detection of several biomarkers such as EpCAM, CD44, VEGF, Mucin 1, CEA has fetched great attention [23]. The electrochemical techniques (amperometry, impedance metric, or potentiometric) deliver a highly sensitive rapid and cost-effective platform for early detection of cancer biomarkers. The miniaturization of electrochemical devices helps in their handy usage. Moreover, the electrochemical techniques can reach to attomole detection level and offer high selectivity [24]. Recent studies have shown the crucial role of nanomaterials in the enhancement of the performance of electrochemical devices for the early detection of cancer [23]. The excellent electrical, mechanical, electrochemical, and optical features of 2D materials have fetched much attention from the past decade in terms of their wide applicability in various fields including disease diagnosis and therapeutics [25]. There are several types of 2D materials such as graphitic carbon nitride [26], transition metal dichalcogenides [27], black phosphorous [28], hexagonal boron nitride (borophene) [29], graphene [30], metal halides [31], metal oxides [32], metal-organic frameworks [33], some polymer [34] which have been investigated for various biosensing applications. Among these, early transition metal carbides and/or nitrides (MXene) are unique in terms of their hydrophilicity, electrochemical, mechanical, and optical properties [35]. They are commonly synthesized using the HF etching method [36]. MXenes are relatively newer when compared to other 2D materials as they were introduced in 2011 at Drexel University. The MXene was usually produced by the etching of the Al element from the MAX phase. MXenes are members of 2D transition metal carbides and carbonitrides [37] and are considered as new generation material currently being used for a wide range of applications [38]. MXene has also been involved in the formation of multifunctional composites such as polymer nanocomposites, carbon nanocomposites, oxide composites.

Recently, MXene has been efficiently used for various biosensing applications [39], targeted drug delivery [40], cancer

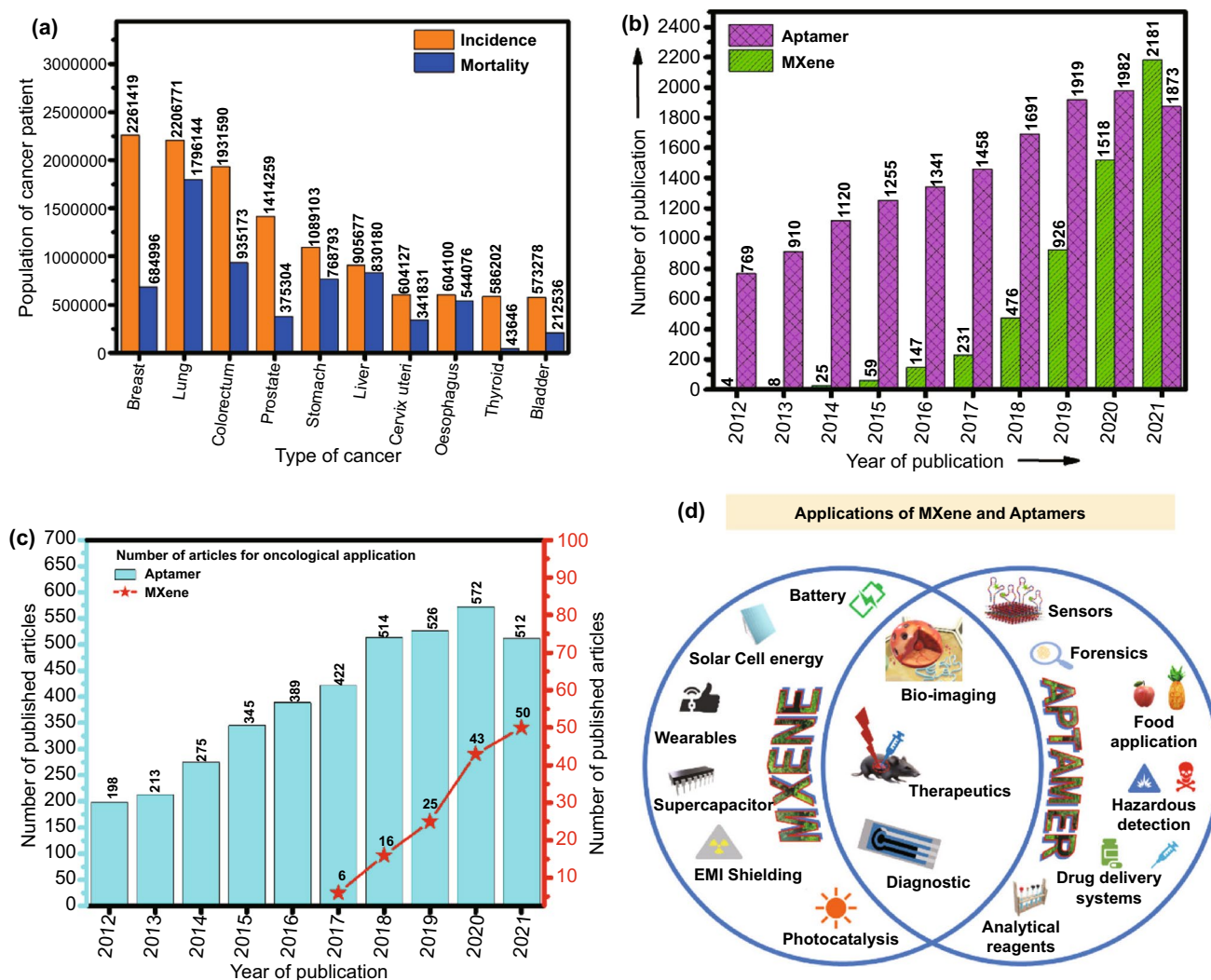


**Fig. 1** Graphical representation of **a** estimated number of incident cases and mortality worldwide, both sexes and all ages (last access date: 10.12.2021); **b** the literature published on aptamer and MXene in last decade; **c** number of literature published for oncological application of aptamer and MXene in last decade (last access date: 16.12.2021). **d** Applications of MXene and Aptamer

therapies [41], energy storage [42–44], heat resistance material synthesis [45], catalysis [46], and many other [47]. The MXenes are considered a promising material in analytical chemistry applications owing to their various unique properties [48]. High surface area, high functionalities on the surface, hydrophilicity, production in large batches, high stability, high conductivity, and non-hazardous nature are some of such properties [49]. Moreover, the properties of the MXenes can be tuned accordingly with the changing size, spacing, and thickness of the layers [50]. The MXenes show excellent biocompatibility [51]. MXene-based electrochemical devices display ultra-high sensitivity of detection of target analyte and have shown potential for the detection of cancer biomarkers [52].

In the last few years, the use of MXenes has been increased exponentially for various biomedical sensing applications. As per the data collected from Web of Science, the exponential increase was observed in the number of articles that dealt with MXenes and their usage in oncological applications (Fig. 1b, c). However, the biorecognition elements (BREs) play a crucial role in terms of device reusability, repeatability, stability. In this context, conventional biorecognition elements such as an antibody, enzyme, nucleic acid have their limitations in terms of their stability under ambient conditions. The usage of aptamers in various oncological applications has been well reflected by the number of publications as per the data collected from Web

of Science (Fig. 1). Among the various BREs, aptamers are preferred. Aptamers are single-stranded DNA, RNA, or peptide sequences that specifically bind to the target molecule [53]. Aptamers offer various advantages over other conventional biorecognition elements as they can be applied to a wide range of targets from small molecules, proteins, viruses to whole cells [54]. Aptamers have increased chemical and thermal stability with high affinity and can also be synthesized easily in large batches. Aptamers are also referred to as chemical antibodies as they function as a chemical substitute to the antibody for diagnostic and detection purposes [55]. Aptamers are carefully chosen from the random pools of sequences using the systematic evolution of ligands by exponential enrichment (SELEX) technique [56]. Aptamers-based biosensors are effectively used in biosensing and other therapeutic application; it is also used for the diagnosis and targeted therapy of cancer [57]. Besides, aptamers are widely used in bioimaging, therapeutics, and diagnosis of cancer [58]. In recent studies, aptamer was used for the detection of cancer biomarkers Mucin 1 [59]; it was also successfully utilized for the blocking/inhibition of SARS-CoV-2 [60]. In another study, aptamer was used to detect the circulating biomarkers in cancer patients'

samples such as proteins, nucleic acids, miRNA in body fluids such as blood, urine, and saliva [61]. Besides, the aptamers platform has been used as a delivery vehicle for targeted drug delivery to the cancerous cells as it possesses various advantages like small size, low immunogenicity, high specificity, and they are flexible that it can easily pass through the solid tumors [62]. Moreover, aptamers have successfully been used for wider applications including environmental monitoring, food analysis, hazardous chemical detection, bioanalytical application, viral detection, biomedical research, and therapeutics. MXenes and aptamer share various common applications including bio-imaging (Fig. 1d) [63], therapeutics [64, 65], and diagnosis [66]. Besides their usage in various other applications, as shown in Fig. 1d. The timeline showing the evolution of usage of MXene since its discovery in 2011 to the fabrication of MXene-based aptasensor for cancer diagnostics and therapeutics is shown in Fig. 2. Additionally, the schematic for the fabrication of IoT-enabled smartphone-based electrochemical aptasensors using MXene is shown in Fig. 2. The use of biomarkers along with the aptamer using electrochemical detection technique can be exploited as a boon towards early cancer diagnostics [66–69].

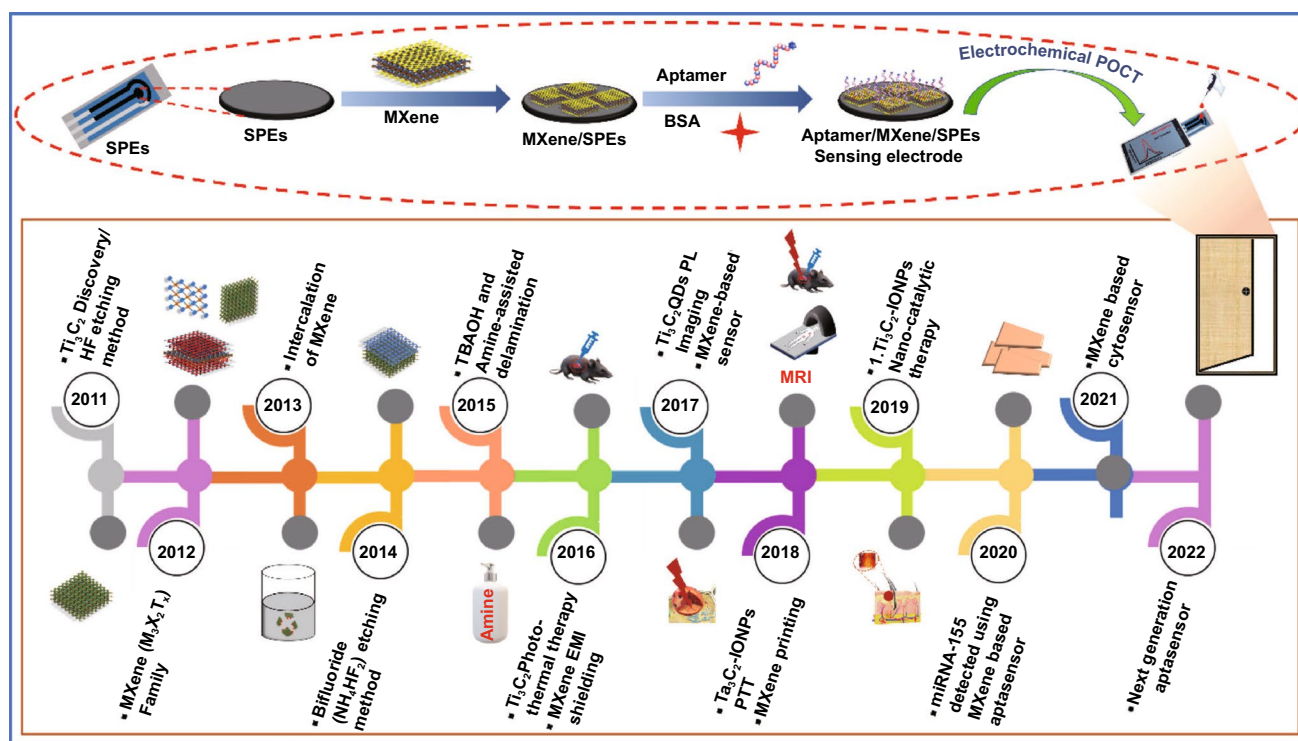


**Fig. 2** Timeline of MXene for the synthesis and its application in the biomedical field

In the present review, we gathered information regarding MXene-based electrochemical aptasensors for the detection of cancer biomarkers. The potential cancer biomarkers for which aptamers are available along with approaches for designing and synthesis biomarker-specific aptamers have been discussed. Various synthetic techniques, as well as post-processing modification of MXenes, have been elucidated, which can be helpful for the development of selective and sensitive aptasensors. In addition, emphasis has been given to properties such as electrical, optical, thermal, chemical stability, and mechanical properties of MXenes. Furthermore, a brief insight over futuristic sensing applications of MXene, as well as difficulties and perspectives, has been presented. The content of this review is expected to improve knowledge and pave the way for the development of future next-generation electrochemical biosensors which could revolutionize the field of disease diagnosis.

## 2 Potential Biomarkers Associated with Cancer

The cancer cells grow rapidly which often led to tumor cell heterogeneity because it exhibits different morphology and behavior. Tumor heterogeneity can be identified using reliable biomarkers. A biomarker is an abbreviation for biological markers associated with a specific disease, and it is measured as an indicator of the extent of clinical diseases [20, 70]. The presence of a biomarker in blood or any other body fluid or tissues indicates the particular condition of disease [71]. Biomarkers can be classified into subtypes based on their application as diagnostic biomarkers, monitoring biomarkers, pharmacodynamic/response biomarkers, predictive biomarkers, and prognostic biomarkers [72]. Diagnostic biomarker assists in knowing disease development and the accomplishment of the treatment. The diagnostic biomarker not only recognizes the person with a certain disease but also classifies the disease [73]. Monitoring biomarkers are used multiple times for evaluating the disease status or patient's condition in response to pharmaceuticals or any other external agent [74]. The pharmacodynamics/response biomarker is those biomarkers whose level changes in response to medicine or any other environmental factors [75]. The predictive biomarkers are used to recognize people which are more likely to be affected either positively or negatively by specific medical products or any other external agents [76]. A prognostic biomarker is a biomarker that predicts

the probability of the occurrence of a clinical condition, its recurrence, or progression in a certain population [33]. Cancer biomarkers can be employed for early diagnosis of a tumor or its reappearance, for prognosis or predicting a patient's response to specific drugs or treatment, or knowing the toxicity of therapeutic interventions [77]. The valuation of biomarkers can be influenced by some factors such as type of tumor whether it is new or recurrent, tumor heterogeneity, and treatment effect [78]. The malignancy and metastasis pathways are the major barriers that limit the conventional therapeutics strategies. Due to tumor heterogeneity, the expression of cancer biomarkers can differ between biopsy tissue and surgical resection specimens in a patient with untreated newly diagnosed cancer. Further, cancer treatment can also cause a change in the expression of biomarkers and the emergence of resistant cancer cells that survive and become prevalent following each treatment. Because tumor DNA is fundamentally unstable, it can change over time, resulting in differences between initial and recurrent/persistent tumors. Because of the primary tumor's treatment and the innate instability of tumor DNA, the molecular phenotype and the biomarkers of primary vs. recurring malignancies can differ [78].

Biomarkers associated with various diseases including cancer can be detected through various approaches. The general approach depends on the basic biology of the tumor and surroundings [79]. With the advancements in technology and more knowledge about the tumor, biomarkers can be identified easily and rapidly using different techniques [80]. Some of the techniques used for the identification and quantification of the biomarker are advanced sequencing, gene expression arrays, and mass spectroscopy [81]. The major challenge is that these techniques produce a vast amount of data that needs to be analyzed. The more focus is on the development of such techniques which can deliver accurate results and avoid further validation.

Various other analytical techniques such as polymerase chain reaction (PCR), immunohistochemistry, flow cytometry have been used for the evaluation of cancer biomarkers; however, they lack acceptable sensitivity and need sophisticated instrumentation facilities with long run time. Biosensors-based detection of biomarkers can be used efficiently for the early diagnosis of cancer disease [15, 20, 23]. The use of biorecognition elements (BREs) such as an antibody, aptamers, enzymes with conjugation to biomarkers associated with cancer cells enhanced the selectivity and sensitivity of the

detection technique [82]. The use of aptamers over conventional BREs biorecognition elements gives promising results with increased selectivity and sensitivity. Moreover, aptamers over other BREs such as antibodies, enzymes, cells are physically, chemically stable, and also, regenerated without losing integrity. Aptamers can be synthesized for a wide range of analytes with high specificity [83]. To date, a variety of aptamers with the ability to bind to the receptors of the once cells have been employed. These include prostate-specific membrane antigen (PSMA), Mucin 1 (MUC1), protein tyrosine kinase-7 (PTK7), VEGF, CA-125, CEA, CD44, and IL-6, etc. [84]. Aptamers designed for the identification and detection of various biomarkers associated with different types of cancer are enlisted in Table 1 along with their sequences and their properties.

### 3 Approaches for Designing of Aptamers

Aptamers are single-stranded synthetic nucleic acids (DNA or RNA sequences) that selectively binds with specific biomarker and can be wrapped into 2D (two-dimensional) and 3D (three-dimensional) structures. Due to 2D and 3D structures, they possess enhanced surface density and reduced spatial blockage and thus show high binding performance toward the target [82, 122–124]. Aptamers are robust molecules in terms of structure and functional aspects and hence remain stable throughout a wide variety of temperatures and other stringent conditions. Unlike antibodies, which need the biological systems for their synthesis, aptamers can be synthesized chemically, remain stable in the pH range of 2–12, and can undergo heat refolding. Another advantage of aptamers is that they can be chemically modified by adding functional groups to match the target molecule's detection requirements [125]. Aptamers can be generated from oligonucleotide libraries via an *in vitro* selection technique called SELEX (Systematic Evolution of Ligands by EXponential Enrichment) [125, 126]. In this process, the aptamers have been selected via an iterative process that involves binding of the target protein/biomarkers with an oligonucleotide in a library followed by washing unbound aptamers and amplification of bound selected oligonucleotide. Multiple cycles of the SELEX process led to the enrichment of highly specific oligonucleotides against a particular target. Afterward, the aptamer with high selectivity was selected, affinity-purified, and sequenced to produce a specific aptamer library [127].

The steps of aptamer synthesis via the SELEX process are shown in Fig. 3a. Cell-SELEX, microfluidics-SELEX, capillary electrophoresis-based SELEX, FACS-based SELEX, magnetic bead SELEX, microtiter plate-SELEX, and *in vivo* SELEX are a few of the SELEX variations that have recently been developed for the improved synthesis of aptamers [127–129]. Figure 3a, b depicts the fabrication of aptasensors along with the advantages of using aptamers over antibodies. The most common biosensor-based diagnostic approaches are optical, electrochemical, and piezoelectric. These biosensors are classified as labeled or label-free aptasensors based on the transduction processes used. The electrochemical sensing techniques can be used for both label-free optical sensors as well as label-based aptasensors [130]. The details of electrochemical aptasensors their design and fabrication strategies are discussed in Sect. 5 of this review.

### 4 MXene: Synthesis and Properties

Owing to the wide application of MXenes', its intrinsic compositional properties are necessary to evolve in distinct directions. These properties, on the other hand, are determined during the synthesis stage and are influenced by a variety of parameters, including the precursor MAX phase, the reaction duration, the etchant, and the temperature of the process. The regulation of these parameters remains a challenge to get appropriately designed MXenes with desired characteristics [131]. Conventional MXene, o-MXene, and i-MXene are the types of MXene [132]. MXenes are produced by a process of selective etching in appropriate solvents or solutions. Etching is generally carried out in acidic solutions [133]. Etching results in surface terminations with the various functional groups making them feasible to be used further [133, 134]. Due to the strong mechanical, optical, and electrical properties, MXene's have attracted attention for a wide range of applications in energy, medicines, and diagnostics [135].

#### 4.1 Structure and Synthesis of MXene

After the discovery of MXene a decade ago, it has gained considerable attention in the research field [37]. The general formula for MXene is  $M_{n+1}X_n$ , while for MAX phase the general formula is  $M_{n+1}AX_n$ , where  $n = 1, 2, \text{ or } 3$ , M is

**Table 1** Cancer biomarkers associated with different types of cancer for which aptamers have been designed and exploited

S. no.	Cancer biomarker	Cancer type	Function and properties	Aptamer sequence	References
1	VEGF- Protein	Breast cancer	Promotes angiogenesis Prognosis	5'-GGG CCG TTC GAA CAC GAG CAT GGT GGG TGG TGG CCC TAG GAT GAC CTG AGT ACT GTC C-3'	[85]
				5'-GCA GCT ATG TGG GGG ACG TCC AGC TGC-FAM-3'	[86]
2	PCA3- Protein PSA	Prostate cancer Prostate cancer	Prognosis Cleave semenogelins in the seminal coagulum	5'-TGG ATA CCG CCG GGT AGA TA-3' 5'-AGUUUUUGGUGUGCCUUUUUGU CCCC-3' 5'-SH-(CH2)6-TTTTTTTTTTTTATTAAAGC TCGCCATCAAATAGCTGC-3' TT-Cy5-3' AATTAAAGTCGCCATCA AATAGCTTT GAGCGGGTTGCTGGGATGATAAGGCC CCTTTGATGCTG	[87] [88]
3	MUC1	Colon, breast, ovarian, lung, and pancreatic cancer	Protect cells from infection	5'-GAGCGGGGTTGCTGGGATGATAAG GCCCTTTGATGCTG-3'	[89]
4	CEA	Colorectal cancer, esophageal cancer, gastric carcinoma, pancreatic carcinoma	Cancer diagnosis and treatment	5'-NH2-(CH2)6-TTT TTA ATT AAA GCT CGC CAT CAA ATA GCT TT-3' 5'-CCGUCAGGUCACGGCAGCGAAGCU CUAGCGCGCCAGUUGC-3' 5'-HS-(CH2)6-ATT AAA GCT CGC CAT CAA ATA GC-3' 5'-NH2-GCAGTTGATCCTTTGGATAACC CTGG- 3'	[89] [90] [91] [92] [93]
5	EpCAM	Colorectal, breast, gallbladder, pancreatic, liver cancer	Cancer diagnosis, prognosis, and therapy	5'-Texas Red -ATACCAGCT TATTCAAATT-3', random ssDNA 5'-TCATTACATGTTTCCT TACTTC CAG-3' SH-ATACCAGCTTATTCAAATT 5'-ATACCAGCTTATTCAAATT-3'	[94] [95] [96] [97]
6	EGFR	Colorectal, breast, ovarian, and colorectal cancers	Promotes cell division and proliferation	5'-/5carboxyl/-CAC TAC AGA GGT TGC GTC TGT CCC ACG TTG TCA TGG GGG GTT GGC CTG-3' 5'-TAC CAG TGC GAT GCT CAG TGC CGT TTC TTC TCT TTC GCT TTT TTT GCT TTT GAG CAT GCT GAC GCA TTC GGT TGA C-3'	[98]



**Table 1** (continued)

S. no.	Cancer biomarker	Cancer type	Function and properties	Aptamer sequence	References
7	IL-6	Lung cancer	Cytokine biomarker regulates immune responses	5'-NH <sub>2</sub> -GGT GGC AGG AGG ACT ATT TAT TTG CTT TTC T -3'	[99]
8	HER2	Lung and breast cancer	Radiation injury biomarkers	5'-SHC6-TTTTT GGGG AAAAA CTT CCAACGGCTCGATTGTCAGCTTTAGT -3'	[100]
		Breast, gastric cancer	Downregulation of HER2 can induce apoptosis by altering cell proliferation and downstream signaling pathways	5'-GCAGCGGTGTGGGG-3'	[101]
				5'-NH <sub>2</sub> -(CH <sub>2</sub> ) <sub>6</sub> -GGG CCG TCG AAC ACG AGC ATG GTG CGT GGA CCT AGG ATG ACC TGA GTA CTG TCC-3'	[102]
				5'-biotin-ACGACCCGATAAGTGCATTAG CACGTCCGAGAAAGCCAGACGGG TCACACAGAGTTA-3'	[103]
				5'-SH-(CH <sub>2</sub> ) <sub>6</sub> -ATTAAGAACCATCA CTC TTCCAAATGGATATACGACTGGG-3'	[104]
				5'-TCT AAA AGG ATT CTT CCC AAG GGG ATC CAA TTC AAA CAG 6 S-S-3'	[105]
				[ThiC6]AACCCGCCAAATCCCTAAGAG TCTGCATTGTCAATTTGTATATGTAT TTGGTTTTGGCTCTCACAGACACACT ACACACGCA	[106]
9	HE4	Ovarian cancer	Early detection	5'-FAM-AGC AGC ACA GAG GTC AGA TG-3', reverse primer 5'-biotin-TTC ACG GTA GCA CGC ATA GG-3', 5'-FAM-AGC AGC ACA GAG GTC AGA TG (N)25 CCT ATG CGT GCT ACC GTG AA-3'	[107]
10	CA125	Ovarian cancer	Early diagnosis	5'-AAAAAACTACTATAGGGAGACAA GAATAAACGCTC AA-3'	[108]
11	CRP	Cancer	Diagnose inflammatory reactions in cancer	5'-CGAAGGGGATTCGAGGGGTGATTG CGTGCTCCATTTGGTGTTTTTTTTTTTT-(CH <sub>2</sub> ) <sub>6</sub> -NH <sub>2</sub> -3' 5'-CGAAGGGGATTCGAGGGGTGATTG CGTGCTCCATTTGGTGTTTTTTTTTTTT-(CH <sub>2</sub> ) <sub>6</sub> -SH-3'	[109]

**Table 1** (continued)

S. no.	Cancer biomarker	Cancer type	Function and properties	Aptamer sequence	References
12	AFP	Hepatocellular, prostate, and ovarian cancer		5'-GGCAGGAAGACAAAACAGCTTGGC GGCGGAAAGGTGTTAAATCCCG GGTCTGCGTGGTCTGTGGTGTGT-3'	[96]
13	CTCs	Hepatocellular cancer,	Used to evaluate cancer metastasis	5'-HS-(CH <sub>2</sub> ) <sub>6</sub> -GTG-ACG-CTC-CTA-ACG- CTG-ACT-CAG-GTG-CAGTTC-TCG-ACT- CGG-ICT-TGA-TGT-GGG-TCC-IGTCCG -TCC-GAA-CCA-ATC-3'	[110]
				5'-dithiol-1-TTTTTTTTTTACAGCATCCCC ATGTGAACAATCGCATTGTGATTGTTA CGGTTTCCGCCCTCATGGACGTGCTG-3'	[111]
				ZY5C aptamer 5'-SHC6TTTTTTTTTTCACGCATAGCCTTT GCTCCTCGTCIGGAACGTCGCAGCTTT AGTTCTGGCCTATGGCTG-3'	[112]
		Ovarian cancer		5'-GCAGGAAGACAAAACA-N40-GGTCTG TGGTGTGT-3'	[113]
				5'-SHCACTACAGAGGTTGGTCTGTCCC ACGTTGTC.ATGGGGGTTGGCCTG	[114]
14	Tg	Thyroid cancer	Diagnosis and postoperative monitoring	Primer sequences (forward 5' -CCTAACCGA TATCACACTCAC-3', reverse 5' -GATACT CCAATGACGACCAAC-3') and the random ssDNA library (82 nt, 5' -FAM-CCTAAC CGATATCACACTCAC-N40- GTTGGT CGTCATTGGAGTATC-3')	[115]
15	NCL	Prostate cancer	Regulation of several mechanisms related to nucleic acid metabolism and tumor prognosis	5'-FAMGTTGGGGTGGTGGTGGTGTG GTGGTGGTGGCCAAC-Dabeyl -3'	[116]
				5'-GGTGGTGGTGGTGGTGGTGGTGGT GG-Rox-3'	[117]
16	AGR2	Pancreatic, breast, ovarian, prostate, and colo- rectal cancer	Early diagnosis	5'-CG <sub>3</sub> TG <sub>3</sub> AGT <sub>2</sub> GTG <sub>9</sub> TG <sub>3</sub> AG <sub>3</sub> T <sub>2</sub> -3'	[118]
17	STP1	Ovarian cancer	Prognosis	5'-ATCCAGAGTGACGCAGCA CGGCAC TCACTCTTTGTTAAAGTGGTCTGCTTCT TAA CCTTCATCGACACGGTGGCTTA-3'	[119]
18	IncPCA3	Prostate cancer	Predict prostatic biopsies	5'- AGUUUUUGCGUGUGCCUUUUUUUGU CCCC-3'SH	[120]
19	PDGF-BB	Breast, pancreatic, prostate, ovarian, and liver	Play a potent role in the growth and metastasis	5'-C <sub>6</sub> -CAG GCT ACG GCA CGT AGA GCA TCA CCA TGA TCC TG-3'	[120]

**Table 1** (continued)

S. no.	Cancer biomarker	Cancer type	Function and properties	Aptamer sequence	References
20	KIT	Cancer		5'-GAG GCA TAC CAG CTT ATT CAA GGG GCC GGG GCA AGG GGG GGG TAC CGT GGT AGG ACA TAG TAA GTG CAA TCT GCG AA-3'	[121]
21	PTK7	Breast, lung, colon, and gastric cancer	plays important role in cell regulation, ion transport, and cancer development	5'-H2N-ATC TTA CTG CTG CGC CGC CGG GAA AAT ACT GTA CCG TTA GAT TTT TTT TTT-3'	[122]
22	Thy-1	Pancreatic ductal adenocarcinoma	Facilitate the attachment of tumor cells to endothelial cells and promote tumor metastasis	5'-CAGGGGACGCCACCAAGG-TTGCCG ACAGAWCYGTGGAAGCCGAACCCG GTGCWAGXCGYG-CCATGACCCCGG TGCTG-3' 5'-CAGGGGACGCCACCAAGG-TTGCCGACC YCCYGTGGGGCCACAGAGCAGCAGT GXCGYG-CCATGACCCCGGTGCTG-3' 5'-CAGGGGACGCCACCAAGG-TTGCCG ACCGWACYGTGAGGXCGAACTACA GGCAGXCGYG-CCATGACCCCGG TGCTG-3'	[123]

an early transition metal (Ti, V, Nb, Mo, Cr, Ta, Hf), A is group 13 or 14 elements, and X is mostly C and/or N [136]. There are about 70 MAX phases known (such as  $Ti_2AlC$  and  $Ti_3AlC_2$ ), and many new combinations are being discovered day by day (e.g., the quaternary ordered MAX phases) and related materials [130, 131, 136]. In the MAX phases,  $M_{n+1}X_n$  are the stable layers, whereas the A layer is comprised of weaker bonds. The etching of the Al layer from the MAX phase ( $Ti_3AlC_2$ ) gives rise to  $Ti_3C_2$  (MXene) [137]. The suffix “ene” to the MXene shows that MXene properties are similar to another popular 2D material graphene [138]. MXenes possess excellent physical and chemical properties including low density, high hardness, good resistivity against corrosion, high conductivity [139]. The various compounds of MXenes can be categorized into different categories based on the complexity of the structure. The MAX phase is an MXenes precursor with the stoichiometry  $M_{n+1}AX_n$ , where  $n = 1, 2, \text{ or } 3$ , and “M” is a metal which belongs to the d-block transition metal family, “A” is a group 13 or 14 elements (e.g., Si, Ge, Al, or Sn), and “X” can be carbon, nitrogen, or both. The layers “M” and “A” are intercalated in between phases, which have a hexagonal structure. The “X” atoms occupy the octahedral positions created by the “M” elements [44]. A detailed insight into the structure of MXene is shown in Fig. 4a. The removal of “A” elements from the MAX phase led to the production of multi-layer MXenes which upon intercalation produces intercalated MXene that can be exfoliated or undergo delamination. The steps are depicted in Fig. 4b. Taking the properties of MXene into consideration, recent studies have employed all OD, 1D, 2D, and 3D dimensions of MXene. For instance, 0D MXene  $Ti_3C_2T_x$  quantum dots used for ultra-fast and ultra-narrow laser fibers manufacturing [140], 1D MXene fibers/CoNi/C has been used as microwave absorbers [141], 2D  $Ti_3C_2$  MXene nanosheets for biosensing and photothermal therapy [137], and 3D MXene architecture (3DMA) used for highly efficient solar steam generation (Fig. 4c) [142]. The accessibility of a large surface area of material for interaction, selective binding, and the ability to transduce the binding of analyte into the recognizable signal is the ideal properties of sensing material. The 2D materials exhibit a large surface-to-volume ratio when compared to 0D, 1D, and 3D analogs for material analyte interaction which ensures high sensitivity at an extremely low concentration of target analyte [143]. Their unique features, which result from a rare blend of ceramic and metallic behaviors, have grabbed

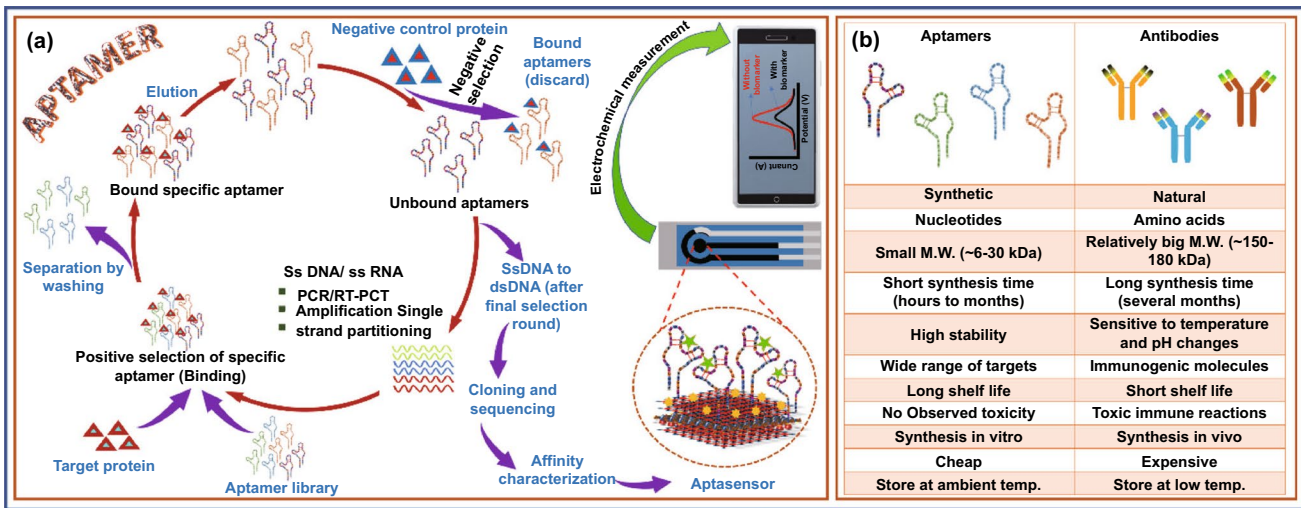


Fig. 3 a Synthesis method for aptamer and detection through electrochemical method, b comparison of aptamers and antibodies as biorecognition element

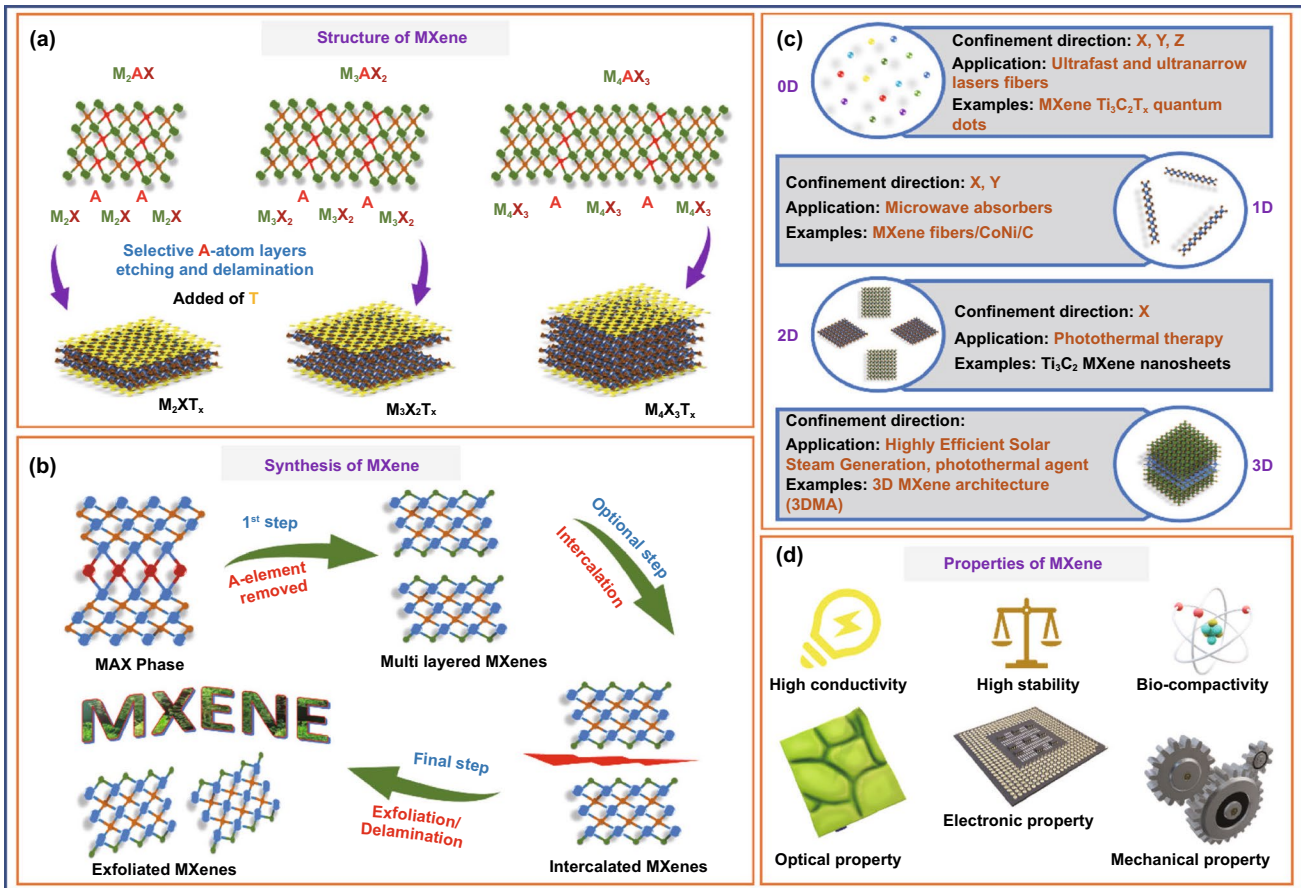


Fig. 4 a Structure of MXene. b Synthesis of MXene. c Dimensional-based classification. d Properties of MXene

much research interest. MAX phases have high hardness, low density, and high corrosion resistance, akin to ceramics, while also having high electrical and thermal conductivities and enhanced machinability which mimics metallic material [143, 144]. A schematic of desirable properties of MXene is depicted in Fig. 4d.

The fundamental bonds are responsible for these revolutionary properties, whereas M–X bonds include a mixture of ionic and covalent interactions. The nature MA bonds are entirely metallic. As a result, unlike other 3D layered materials like transition metal dichalcogenides and graphene, which have weak interactions, MAX phases have robust bonds that provide stability and inhibit cleavage by shearing or other mechanical means. Initially, the chemical exfoliation method allowed the creation of MXene-based 2D materials from primary bonded MAX phases [37].

Due to low cost, simplicity, and scalability, high-temperature synthesis of MAX phase from binary elements is the most commonly used procedure. In this method, TiC, Ti, and Al powders are mixed in ball milling (Fig. 5a, b) and then annealed in a tube furnace under an inert atmosphere in presence of argon at 1400 °C for 2 h with a rate of heating and cooling of 3 °C min<sup>-1</sup> (Fig. 5c). Afterward, the material was ground, milled, and drilled using pestle mortar followed by sieving to yield a powder of known particle size. The powder

was subjected to HCL wash to remove impurities (metallic and intermetallic) before sieving (Fig. 5d) [145].

Various synthesis techniques have been introduced which contributed significantly to the field of MXenes' research to meet the appropriate requirement for various applications. Etching and delamination are extensively used as prime methods for the synthesis of MXenes [146]. In the precursor MAX phase, the etching procedure is primarily used to disrupt the M–A metal bond. Fluorine-containing acid etching [34, 147], halogen etching [148], strong alkaline etching [149], high-temperature etching [150], and electrochemical etching [151] are the different types of etching methods used so far. The most popular technique for etching the A layer is to use a hydrofluoric acid (HF) or a strong alkali. Many sagging bonds arise on the surface of 2D MXene nanosheets as a result of this process, which is converted into numerous terminations in groups such as –F, –O, and –OH. In the meantime, the MXene nanosheets are exposed to more or lesser flaws during the reaction, making it easier for the material to deteriorate and lose its original properties [152], while in the delamination method, under the influence of mechanical force [37] or chemical intercalants [153], multilayer MXenes peel apart to generate single- or few-layer lamellae in the delamination stage. The extreme vibrations caused by ultrasound, on the other hand, cause a shrink of

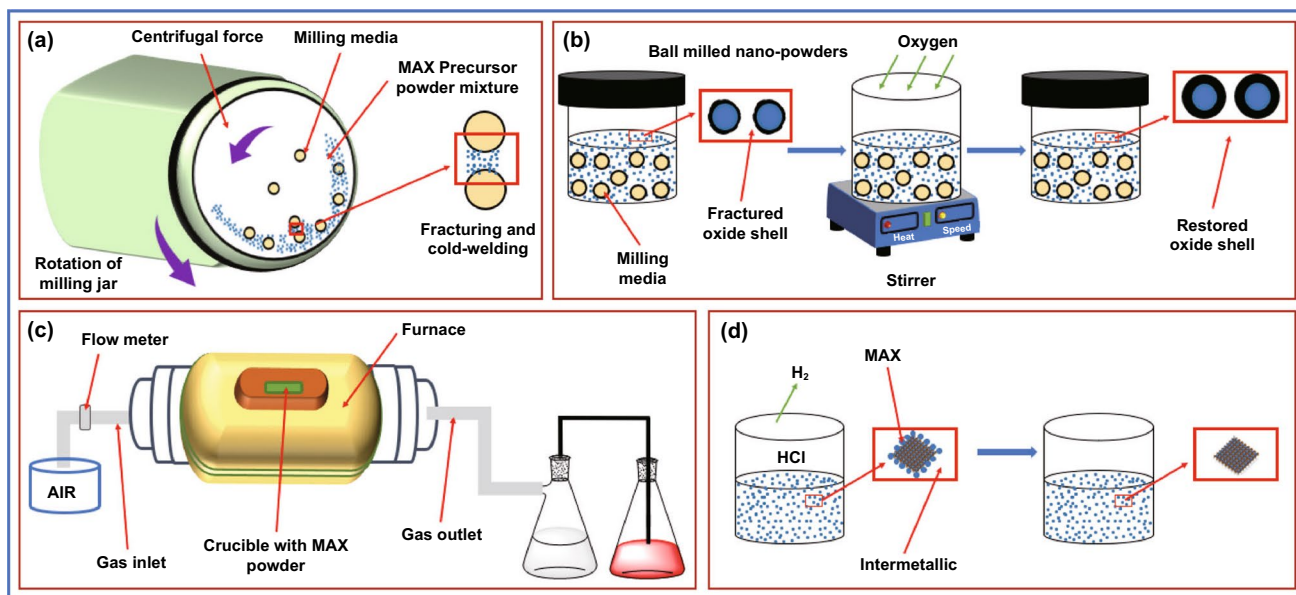


**Fig. 5** Steps associated with the production of the MAX phase: **a** ball milling, **b** passivation by oxygen, **c** high-temperature synthesis, and **d** acid washing to remove interferences

the size of the MXene nanosheet which led to a loss of electrical and mechanical characteristics. Chemical intercalation allows MXenes to be reduced in size to some extent, but it is tough to eliminate these chemical agents in successive operations, which affect the conductivity of MXenes films significantly [154]. As a result, MXenes' real properties deviate significantly from their theoretical values, restricting their uses in several areas such as energy storage [155], catalysis [156–158], electromagnetic shielding [40, 45, 48, 158, 159], flexible electronics [160], and chemical sensing [161]. Based on literature several methods of MXene synthesis can be categorized into top-down [133], wet chemical [148], and bottom-up [162] approaches. The detailed insight of each method is illustrated in Fig. 6. The top-down method is the most preferred approach for the synthesis of MXene. In this method, etching of A elements from the 3D, MAX phase was carried out using HF (Fig. 6a), while in the bottom-up method the MXene is constructed using small organic or inorganic molecules (Fig. 6b). The bottom-up method provides the advantage of controlled synthesis with appropriate size and morphology and surface terminations

when compared to the top-down method. Further, in the wet chemical method, anodic etching was performed followed by delamination (Fig. 6c). The precautions taken during the synthesis of the MAX phase and MXene remain a concern among the scientific community as it uses acid and high temperature. The safety measures such as PPEs kit, gloves, fume hood, and proper handling of acid and water while synthesis of MXene should be properly taken care of. The safety measures should be followed in general, while acid and other corrosive chemicals are shown in Fig. 6d.

An ultrafast polyaniline@MXene cathode was created by casting a homogeneous polyaniline layer onto a 3D porous  $Ti_3C_2T_x$  MXene; by Li et al., PS spheres with a negative surface charge can disperse homogeneously in water with the same negatively charged  $Ti_3C_2T_x$  MXene flakes (Fig. 7a), which can then be vacuum-assisted filtered into a flexible PS@ $Ti_3C_2T_x$  film (6 m) with  $Ti_3C_2T_x$  MXene flakes wrapping the PS spheres' surface (500 nm). A freestanding and flexible 3D microporous  $Ti_3C_2T_x$  (3D M- $Ti_3C_2T_x$ ) film with an open and interconnected structure was developed after eliminating the PS by thermal annealing at 450 °C

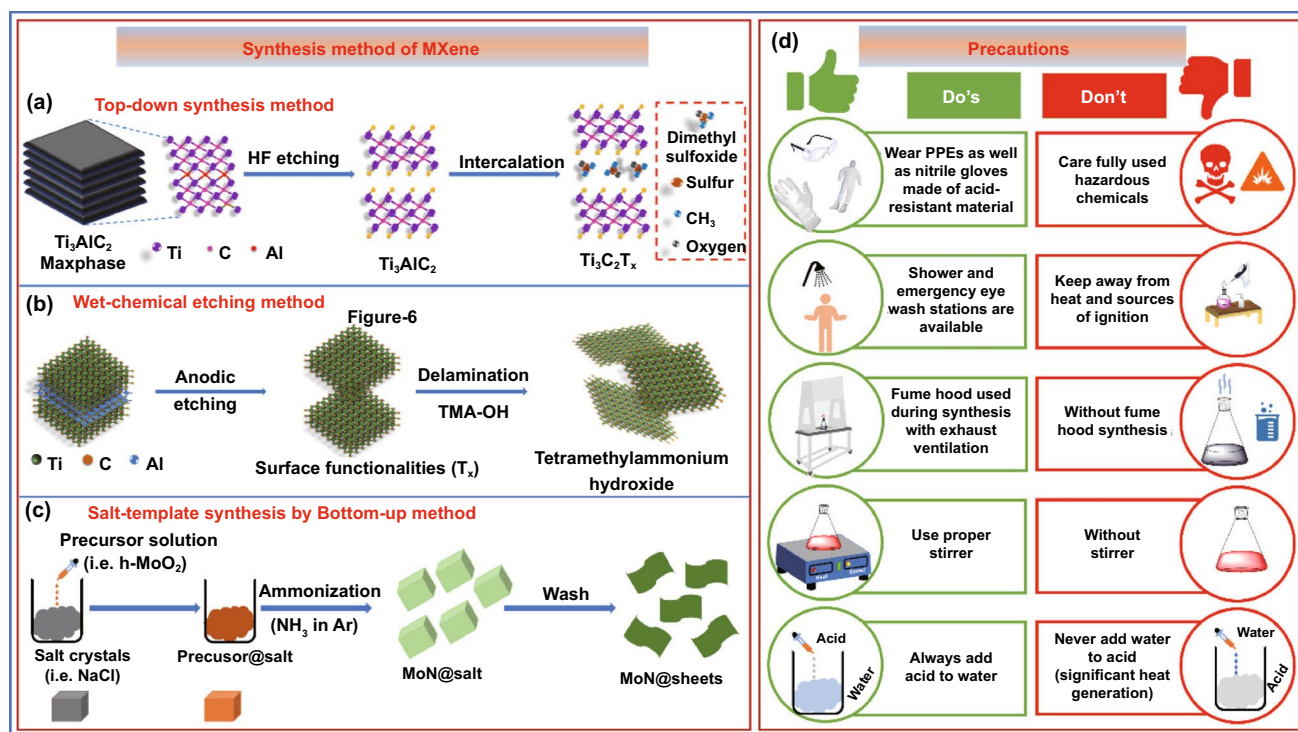


**Fig. 6** Synthesis method of MXene. **a** Top-down synthesis method, **b** wet chemical etching method, **c** salt-template synthesis by the bottom-up method, **d** safety measures and general instructions for laboratory

in argon. This film displayed an electrical conductivity of  $600 \text{ S cm}^{-1}$ , which is higher than a 3D graphene film with a comparable structure ( $12 \text{ S cm}^{-1}$ ) (Fig. 7a) [163]. Lipatov et al. described a new synthetic approach for making high-quality monolayer  $\text{Ti}_3\text{C}_2\text{T}_x$  flakes. In this work, two varieties of  $\text{Ti}_3\text{C}_2\text{T}_x$  flakes were created.  $\text{Ti}_3\text{C}_2\text{T}_x$  was manufactured following the Route 1 method, which involved soaking  $\text{Ti}_3\text{AlC}_2$  powder in a LiF-HCl solution with a molar ratio of LiF to MAX of 5:1. This approach produces mostly monolayer flakes. The molar ratio of LiF to MAX was increased to 7.5:1 in the modified technique in the method opted in Route 2 which provides an excess of  $\text{Li}^+$  ions for intercalation. Herein, the HCl to LiF ratio was doubled to enhance aluminum etching. Further, the delamination of  $\text{Ti}_3\text{C}_2\text{T}_x$  particles created using Route 2 did not require sonication. The key distinctions between Routes 1 and 2 along with the atomic force microscopy (AFM) images which were used to examine the thickness and morphologies of the flakes

produced by both procedures are shown in Fig. 7b. The AFM images revealed that the  $\text{Ti}_3\text{C}_2\text{T}_x$  flakes synthesized by Route 2 are much larger than those produced by Route 1 (Fig. 7b) [164]. Alhabeab et al. produce titanium carbide ( $\text{Ti}_3\text{C}_2\text{T}_x$ ), the most researched MXene, utilizing several etchants and delamination processes. They also discuss the implications of synthesis settings on  $\text{Ti}_3\text{C}_2\text{T}_x$  size and quality, as well as the best procedures for the application. Low concentrations of HF (5 wt%) for 24 h were shown to be just as effective as higher concentrations (10 wt. percent HF for 18 h and 30 wt. percent HF for 18 h), as confirmed by energy-dispersive X-ray (EDX) analysis and X-ray diffraction (XRD) patterns (Fig. 7c) by a shift of the (002) peak of  $\text{Ti}_3\text{AlC}_2$  from  $9.5^\circ$  to  $9.0^\circ$  for  $\text{Ti}_3\text{C}_2\text{T}_x$  and no residual  $\text{Ti}_3\text{AlC}_2$  peaks after etching for 5, 10, and 30F- $\text{Ti}_3\text{C}_2\text{T}_x$ . Further, the elimination of Al in  $\text{Ti}_3\text{AlC}_2$  and the insertion of surface terminations (expressed as  $\text{T}_x$ ) in  $\text{Ti}_3\text{C}_2\text{T}_x$  (e.g., -F, -O, -OH) result in a reduced peak shift of the basal

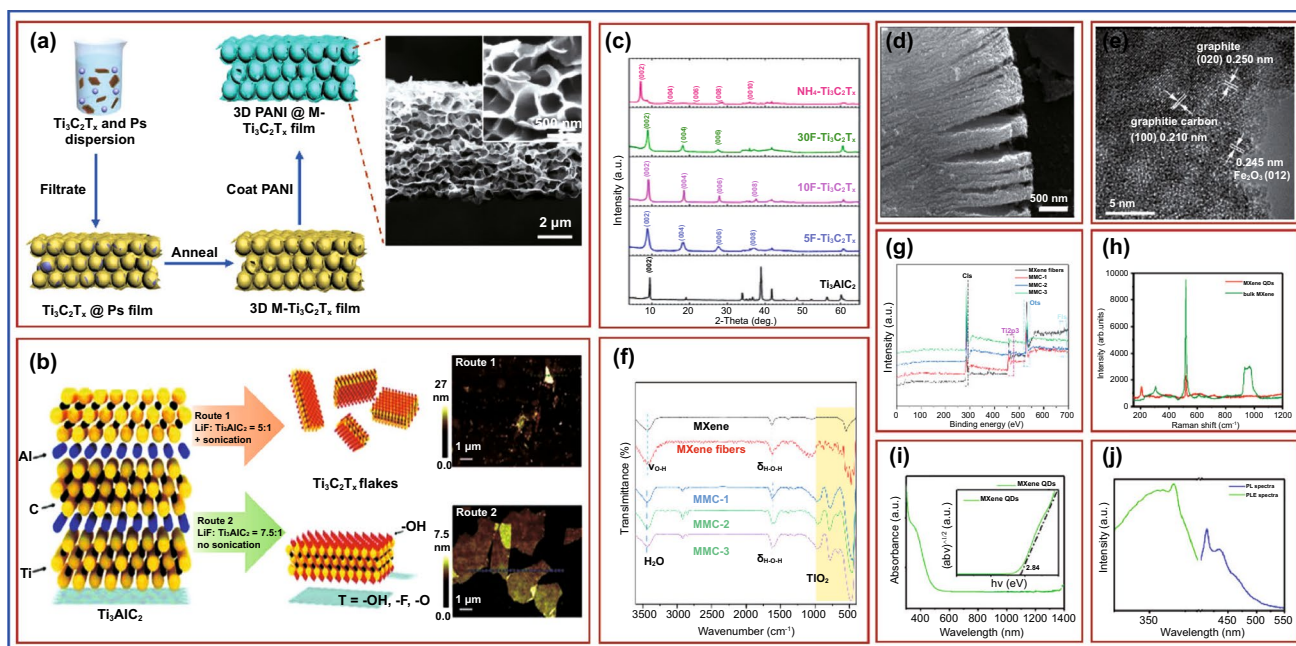


**Fig. 7** **a** Schematic representation of the preparation of 3D macroporous PANI@M- $\text{Ti}_3\text{C}_2\text{T}_x$  frameworks with PS spheres as a template, inset showing SEM images of the formed 3D PANI@M- $\text{Ti}_3\text{C}_2\text{T}_x$  film. Copyright from Ref. [163]. **b** Synthesis of  $\text{Ti}_3\text{C}_2\text{T}_x$  via two different routes with or without sonication, inset showing AFM images of the synthesized  $\text{Ti}_3\text{C}_2\text{T}_x$  flakes. Copyright from Ref. [164]. **c** XRD patterns of  $\text{Ti}_3\text{AlC}_2$  powder and  $\text{Ti}_3\text{C}_2\text{T}_x$  MXene powders synthesized with 5, 10, and 30%wt HF and in situ HF by using  $\text{NH}_4$ - $\text{Ti}_3\text{C}_2\text{T}_x$  routes. Copyright from Ref. [165]. **d** The SEM image of MXenes at 500 nm. Copyright from Ref. [166]. **e** HR-TEM images of  $\text{Ti}_3\text{C}_2\text{T}_x$ @FePcQDs hybrid structure. Copyright from Ref. [167]. **f** FTIR spectrum, **g** XPS spectra of various samples. Copyright from Ref. [141]. **h** Raman spectra of bulk MXene and MXene quantum dots. **i** UV-Vis absorption spectrum of MXene QDs; the inset showing the value of the bandgap fitted. **j** Excitation and emission spectra of MXene QDs. Copyright from Ref. [140]

planes ((002) peak) [165]. The MXenes were characterized using scanning electron microscopy (SEM). As shown in Fig. 7d, the MXenes had a dense layer and an accordion-like shape [166]. The high-resolution transmission electron microscopy (HR-TEM) picture of the  $\text{Ti}_3\text{C}_2\text{T}_x$ @FePcQD nanohybrid (Fig. 7e) revealed interplanar distances of 0.25, 0.245, and 0.21 nm, respectively, corresponding to the (020) plane of graphite, the (012) planes of hexagonal  $\text{Fe}_2\text{O}_3$ , and the crystallographic (100) plane of graphitic carbon. In the synthesis of FePc QDs,  $\text{Fe}_2\text{O}_3$  nanoparticles and carbon dots were produced concurrently at 180 °C. The findings suggested that FePc QDs and  $\text{Ti}_3\text{C}_2\text{T}_x$  nanosheets can be successfully integrated [167]. FTIR spectra of MXene and MXene fiber are shown in Fig. 7f. The X-ray photoelectron spectroscopy (XPS) curves of each group of samples are shown in Fig. 7g. The typical peaks of C 1s (285 eV), Ti 2p (459 eV), and O 1s (530 eV) were visible [141]. The bulk MXene and MXene QDs were also characterized using Raman spectroscopy. From 200 to 1100 cm, the spectrum has six conspicuous peaks (Fig. 7h), which is consistent with earlier findings. The peak of about 500 cm, on the other hand, represents the signal of the Si substrate, as shown in several test results. The optical quality of MXene  $\text{Ti}_3\text{C}_2\text{T}_x$  QDs as investigated using UV–Vis absorption spectroscopy is shown in Fig. 7i. The bandgap is calculated as 2.84 eV by mapping the absorption to the band edge. A fluorescence spectrometer for determining the PLE spectra of MXene QDs and testing their fluorescence properties is displayed in Fig. 7j. As stimulated at 367 nm, the brightest peak appears about 415 and 430 nm [140].

## 4.2 Properties of MXene

High Young's modulus, a tunable bandgap, thermal and electric conductivities are some of the distinctive MXene features. The hydrophilic surfaces of MXenes along with high electrical and thermal conductivities set them apart from the majority of 2D materials [148]. Eventually, specific composition and involvement of different transition metals "M" and "X" elements, and varied functionalization of the surface via chemical and thermal processes led to structure/morphological changes, which can be used to tune their properties and applications performances [163]. The MXenes family's main properties are discussed in this section.

### 4.2.1 Mechanical Properties

Mechanical features of MXenes drew a lot of attention because of the presence of strongest M–C and M–N bonds and two times higher elastic constants ( $c_{11}$ ) than MAX phases [168], and other 2D materials like  $\text{MoS}_2$ , as per the first simulation investigation. Despite having  $c_{11}$  values 2 to 4 times lesser than graphene [36, 166] their bending stiffness is higher [169, 170], indicating that they could be used as composite reinforcements. Thin discs of titanium-based MXenes exhibit hydrophilic behavior with contact angles ranging from 27 to 41 degrees, whereas  $\text{Ti}_3\text{C}_2\text{T}_x$  exhibited a contact angle of 35 degrees [168]. The Young's modulus tends to decrease as the number of layers ("n") increases in both MXene carbides and nitrides [168]. Furthermore, nitride-based MXene compounds have greater values than carbides [171]. The presence of ends reduces the values of elastic constants but upsurges their critical distortions. The significantly higher values of elastic constant of MXene than graphene are a key property for flexible electronics [147]. While there are various mechanical testing methods for the characterization of bulk materials, evaluating the mechanical properties of 2D materials remains difficult. The AFM tip exerts a force at the center of a 2D MXene film in the nanoindentation technique which was used to determine the mechanical properties of 2D nanomaterials [172]. The experimental  $\text{Ti}_3\text{C}_2\text{T}_x$  monolayer Young's modulus of  $333 \pm 30$  GPa was obtained using this technique. Further experimental research should concentrate on developing more controllable synthesis techniques to adjust structural defects, vacancies, and different functional groups, including original molecules [170]. However, overall theoretical and practical analyses of the mechanical properties of MXene and their composites with various functionalization groups still need to be illustrated.

### 4.2.2 Optical Properties

Photocatalytic, optoelectronic, photovoltaic, and transparent conductive electrical devices can be made up of 2D material which absorbs in the range of visible and UV light.  $\text{Ti}_3\text{C}_2\text{T}_x$  films absorbed light in the UV–Vis ranges from 300 to 500 nm wavelength and had a transmittance of up to 91.2 percent at 5 nm thickness [173, 174]. In addition, depending on the film thicknesses, it may have a strong

absorption band at roughly 700–800 nm, which causes pale greenish film color [172] and is important for photothermal diseases (PTT) treatment [175–177]. It is worth noting that the transmittance values could be improved by adjusting the thickness [178] and ion intercalation [174]. The existence of functional groups alters the optical characteristics of these 2D compounds, according to first-principles calculations [179]. In reality, unlike oxygen terminations, fluorinated and hydroxyl terminations have identical properties. When compared to pure MXene, –F, –O, and –OH terminations in MXene lower the absorption and reflectivity in the visible range, while all terminations collectively increase reflectivity in the UV range [179]. The reduction of the size of a lateral flake of MXene has recently been shown to result in decreased absorbance values [180]. A remarkable light-to-heat conversion efficiency (100%) was revealed, which could be advantageous in biomedical applications [181]. To measure the light-to-heat conversion efficiency of  $\text{Ti}_3\text{C}_2$  MXene, a droplet-based light absorption and heat measurement system can be used. In this system an aqueous solution droplet (volume 9.0  $\mu\text{L}$ ) containing MXene is hung at the tip of a PTFE pipet (one-end-sealed), followed by a single-wavelength laser beam irradiation (473 or 785 nm), with specific power density (82 mW) and spot size (0.85 mm in diameter), right in the center of the droplet. The droplet temperature recorded by a precalibrated IR camera in real time. The total temperature profile of the droplet in response to photothermal heating and then natural cooling provides light-to-heat conversion efficiency [182, 183]. Moreover, the internal light-to-heat conversion efficiency of MXene, more specifically  $\text{Ti}_3\text{C}_2$ , was measured to be 100%, demonstrating a flawless energy conversion [181]. Nevertheless, to further enhance MXenes applications, several optical-associated qualities such as plasmonic, luminescence efficiency, and nonlinear optical properties must be unraveled [178–181, 184].

#### 4.2.3 Thermal Properties

The studies on thermal conductivities in terms of thermal expansion coefficients of MXenes are still sparse, despite their importance for electrical and energy-related heat dissipation devices [155]. Simulation studies indicated low thermal expansion coefficients [37, 184, 185] and superior heat

conductivities of MXene-based materials than phosphorene and  $\text{MoS}_2$  monolayer [184, 186, 187]. It was observed that the thermal conductivities of oxygen-terminated compounds rise with the metal “M” atomic number [119, 184]. The edge Green’s function of the semi-infinite  $\text{Mo}_2\text{MC}_2\text{O}_2$  lattice is generated using the MLWFs, the imaginary component of which yields the local density of states (LDOS), from which the energy dispersion of the edge states is determined. The LDOS on the zigzag edge of  $\text{Mo}_2\text{HfC}_2\text{O}_2$  is shown in Fig. 8a, where a pair of topological edge states join the bulk conduction and valence bands to produce a single Dirac cone at the M point.  $\text{Mo}_2\text{TiC}_2\text{O}_2$  and  $\text{Mo}_2\text{ZrC}_2\text{O}_2$  produce similar results [188]. Only  $\text{Ti}_3\text{C}_2\text{T}_x$  thermal conductivity was measured in the laboratory; thus, conductivities of other MXene-based compounds should be investigated. Furthermore, the studies on the relationship between particle size and thermal conductivity that underlines the need for morphological control and optimization in MXenes synthesis need to be explored further.

#### 4.2.4 Magnetic Properties

The MXenes can be magnetized; unlike MAX phases, several investigations carried out to evaluate their magnetic characteristics are projected to have magnetic moments. F functional groups make  $\text{Ti}_3\text{CNT}_x$  and  $\text{Ti}_4\text{C}_3\text{T}_x$  non-magnetic [189], whereas OH and F groups make  $\text{Cr}_2\text{CT}_x$  and  $\text{Cr}_2\text{NT}_x$  ferromagnetic at ambient temperature [190], and  $\text{Mn}_2\text{NT}_x$  is ferromagnetic regardless of surface terminations [191]. For  $\text{Cr}_2\text{CF}_2$  and  $\text{Cr}_2\text{CFCl}$ , the distance between MXene and substrate is 2.76 and 2.57 Å, respectively, showing only a weak van der Waals bonding. As seen in Fig. 8b,  $\text{Cr}_2\text{CF}_2$  and  $\text{Cr}_2\text{CFCl}$  on SiC(0001) retain the compensated anti-ferromagnetic coupling. The DOS of  $\text{Cr}_2\text{CF}_2$  with a symmetrical distribution implies that there is no spin polarization, whereas  $\text{Cr}_2\text{CFCl}$  retains the BMSAF characteristics. These findings reveal that imperfectly functionalized Janus  $\text{Cr}_2\text{CXX}'$  MXenes retain BMSAF properties even when they interact with the substrate, which is significant for nanoelectronic device applications [192, 193]. The reported magnetic moments are, however, simply computational predictions that have yet to be confirmed empirically. It can be due to a lack of information on surface chemistry [194] and limited synthesis of MXene compounds.

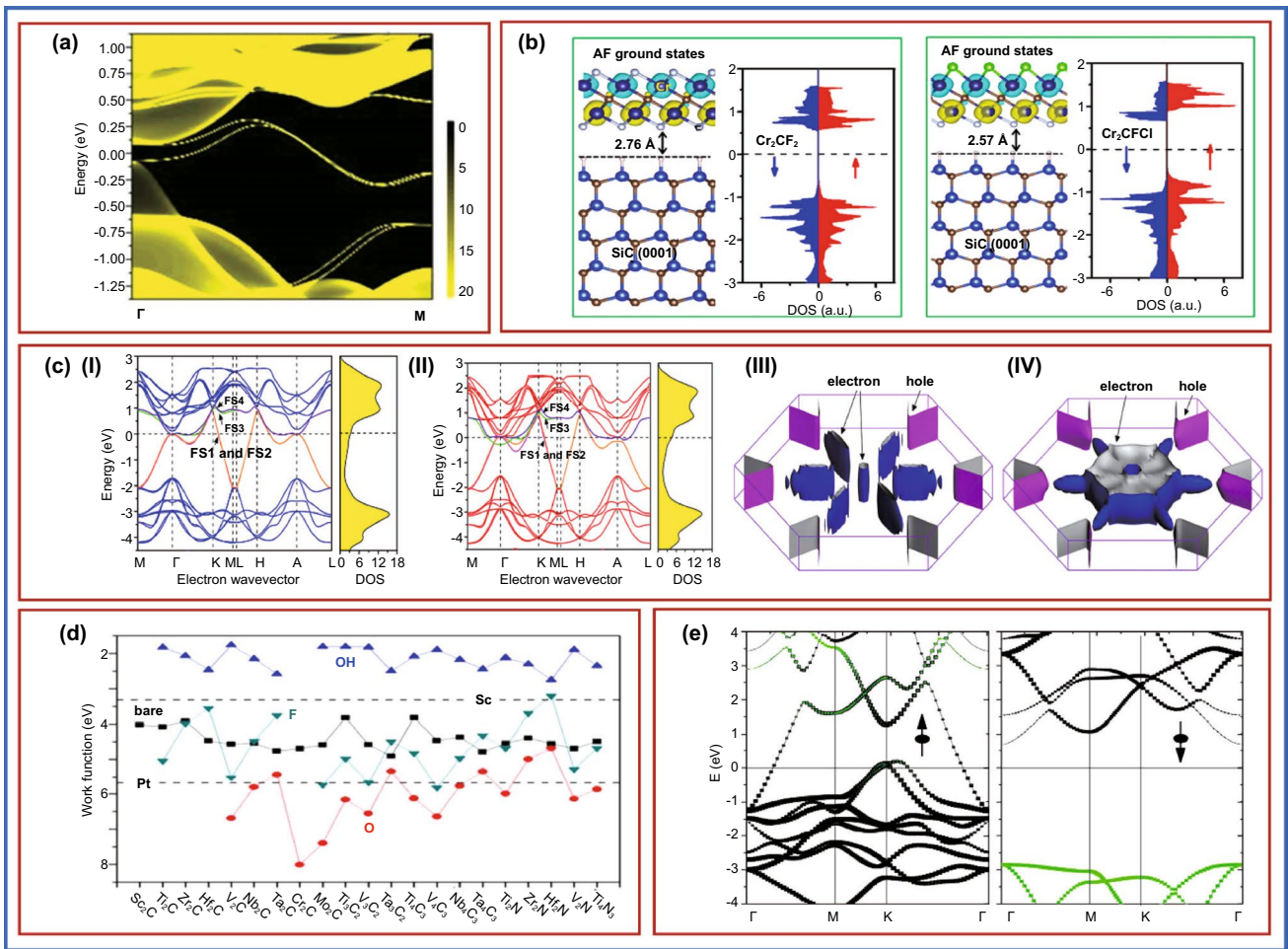


**Fig. 8** **a** Local density of states for  $\text{Mo}_2\text{HfC}_2\text{O}_2$  on the zigzag edge. The edge states connecting the bulk valence and conduction bands form a single Dirac cone at the M point. Copyright from Ref. [188]. **b** The density of states of  $\text{Cr}_2\text{CF}_2$  (left panel) and  $\text{Cr}_2\text{CFCI}$  (right panel) supported on the  $\text{SiC}(0001)$  substrate. Copyright from Ref. [192]. **c** Band structure and Fermi surface. Band structure and **(III, IV)** corresponding FS of **(I, II)** Bernal and **(II, IV)** SH  $\text{Ti}_3\text{C}_2(\text{OH})_2$ . FS1 (magenta) and FS2 (orange) partially degenerate. FS3 (green) and FS4 (violet) are partially degenerated. Copyright from Ref. [200]. **d** Work functions of MXenes with various terminations. For comparison, the work functions of Sc and Pt are also shown by dashed lines. Copyright from Ref. [201]. **e** Band structure for  $\text{Cr}_2\text{C}$  MXene. The weights of the Cr *d* are represented in black and C *p* orbitals are represented in green. Copyright from Ref. [202]

### 4.2.5 Electrical Properties

Several functional groups, their stoichiometry, and ability of solution formation all can be used to adjust the properties of MXenes. MXenes-pressed discs had greater electric conductivities than reduced graphene oxide and carbon nanotubes [167, 181] and were similar to multi-layered graphene. Furthermore, the number of layers in MXene and the presence of functional groups were found to improve resistivity values [195, 196]. As a result, the simulated conductivities are typically higher than those measured experimentally [197]. The defect concentration, delamination yield, d-spacing

between MXenes flakes, surface functional groups, and their lateral sizes produced by each etching procedure play a crucial role in determining the electrical conductivity of MXene. The measured electrical conductivities of  $\text{Ti}_3\text{C}_2\text{T}_x$  ranged from 850 to 9880  $\text{S cm}^{-1}$  [171, 176, 195, 196]. In general, MXenes with lower HF concentrations and etching periods have fewer flaws and bigger lateral diameters, resulting in enhanced electronic conductivity [198]. The higher flake sizes resulted in enhanced conductivities than small-sized MXenes [50]. Furthermore, relative humidity sensing material [199] may impact their conductivities. Thermal and alkaline treatments for surface modification of material

are a good way to improve electrical characteristics. The change and/or alteration of functional groups (particularly F) and intercalated molecules are responsible for the rise by two orders of magnitude [178]. In momentum space, band structure describes the relationship between electronic energy and electron wavevector. The electronic band structure is the most convenient way to describe the microscopic action of electrons in a material. The band structures and density of states (DOS) in specific orientations of the Brillouin zone are depicted in Fig. 8c. The dispersion of the bands perpendicular to the basal planes (ML) is almost low, indicating that the electronic structures are essentially 2D. The conductivity is anisotropic due to the anisotropy of the band structures around and below the Fermi energy (EF). Because the electronic transport properties are determined by electrons near EF, Ti's 3d electrons play a major role in electronic conduction. The form of the entire Fermi surface, which determines transport parameters such as conductivity, is visible in Fig. 8c. Four double-degenerate half-filled bands spanning EF in the band structure correspond to this. In reciprocal space, both FSs show a hexagonal electron pocket around the  $c^*$  axis, surrounded by six cylindrical hole pockets. The hole-like pockets in the FSs of the two layouts are very similar: Around H and K are cylindrical hole pockets [200]. Work functions of MXenes with various terminations are shown in Fig. 8d (for comparison, work functions of Sc and Pt are depicted by dashed lines) [201]. Band structure for  $\text{Cr}_2\text{C}$  MXene is shown in Fig. 8e. Herein, the weights of the Cr  $d$  are represented in black, and C  $p$  orbitals are represented in green [202]. The electrical characteristics of MXenes are connected to the composition of their ingredients and the number of surface termination as per density functional theory (DFT) [203]. Surface terminations of carbides are crucial being semiconductors in the MXenes family; however, some carbonitrides with additional electrons can increase band structure modification and transition to a metallic state.  $\text{Ti}_3\text{C}_2(\text{OH})_2$  and  $\text{Ti}_3\text{C}_2\text{F}_2$  were tentatively anticipated to have modest bandgaps between 0.05 and 0.1 eV, respectively, until Yury Gogotsi and his team found MXenes [204]. Besides, mixed terminations such as  $-\text{F}$ ,  $-\text{OH}$ , and  $-\text{O}$  populate the MXene's surface at random, causing electronic state localization and altering their electrical and other characteristics. As a result, from a theoretical standpoint, modifying the element composition along with surface termination of MXenes can be used to accomplish targeted control of electrical properties. The MXene films

are multilayer stacked macroscopic nanosheets for which electrical characteristics are determined by the intercalation between layers. For example, cations from reagents [205] (tetramethylammonium ion ( $\text{TMA}^+$ ), lithium-ion ( $\text{Li}^+$ ) and ammonium ion ( $\text{NH}_4^+$ )) and organic molecules [206] (isopropylamine and dimethyl sulfoxide (DMSO)) when intercalated into the MXenes layer, led to the modification of their electrical characteristics. As a result, post-processing modifications can successfully alter the surface termination, elemental composition, and intercalation of MXene films, allowing for focused control of their electrical properties.

## 5 MXene-Enabled Advanced Electrochemical Aptasensors for Cancer Diagnostics

MXene, a 2D nanomaterial with plausible electroconductive properties, has been identified as a viable molecule for the fabrication of electrochemical biosensors due to its simple manufacturing process. Aptamers, on the other hand, have proven to be a boon for manufacturing low-cost sensing devices due to their great selectivity and specificity, as well as their mass production ability. The advantageous electroconductive properties of MXene enabled with selective and specific aptamers against cancer-specific biomarkers can be potentially employed for early and efficient diagnostics of cancer which is the need of an hour. In this section, we have discussed the studies on MXene-enabled electrochemical aptasensors for the detection of cancer-specific biomarkers. For the synthesis of various types of MXene composite, Naguib et al. added the  $\text{Ti}_2\text{C}$ ,  $\text{Ta}_4\text{C}_3$ ,  $\text{TiNbC}$ ,  $(\text{V}_{0.5}, \text{Cr}_{0.5})_3\text{C}_2$ , and  $\text{Ti}_3\text{CN}_x$ , where  $x < 1$  which expands the MXenes family [207]. In further work, Naguib et al. proved that MXenes can also be used as electrodes when intercalated with Li ions in lithium-ion batteries [208]. Aptamer-enabled MXene-based electrochemical biosensors have been used in recent studies to detect a variety of cancer biomarkers, as stated in Table 2. In a recent study, the breast cancer marker Mucin 1 was detected using a competitive electrochemical aptasensor fabricated on a cDNA-ferrocene/MXene probe (MUC1). Herein, MXene ( $\text{Ti}_3\text{C}_2$ ) nanosheets with high specific surface area and excellent electrical conductivity were chosen as aptamer-probe carriers. To make a cDNA-Fc/MXene probe, ferrocene-labeled complementary DNA (cDNA-Fc) was coupled to the surface of MXene followed by attachment of MUC1 aptamer on the electrode via Au-S bonds. A cDNA-Fc/MXene/Apt/Au/GCE aptasensor was made and

**Table 2** MXene-based electrochemical aptasensors for cancer diagnosis (sensitivity and detection limit)

S. no.	Material	Biomarker	Sample	Technique	Linear range	LOD	References
1	MXenes-BPQDs@ Ru(dcbpy) <sub>3</sub> <sup>2+</sup> -PEIAb <sub>CD63</sub>	Exosomes, CD63		CV	1.1 × 10 <sup>2</sup> to 1.1 × 10 <sup>7</sup> particles μL <sup>-1</sup>	37.0 particles μL <sup>-1</sup>	[166]
2	0D/2D Ti <sub>3</sub> C <sub>2</sub> T <sub>x</sub> @ FePcQD nano-hybrid	miRNA-155	Serum	EIS	0.01 fM to 10 pM	4.3 aM	[167]
3	cDNA-Fc/MXene/Apt/Au/GCE aptasensor	Mucin 1	Serum	SWV	1.0 to 10 μM	0.33 pM	[209]
4	MPA-CdS:Eu NC	Exosomes, CD63	Serum	EIS, ECL	3.4 × 10 <sup>5</sup> to 1.7 × 10 <sup>8</sup>	7.41 × 10 <sup>4</sup> particles mL <sup>-1</sup>	[210]
5	Ti <sub>3</sub> C <sub>2</sub> MXene (MXene)	Exosomes, CD63	Cancer cells and Serum	CV, EIS	5 × 10 <sup>2</sup> to 5 × 10 <sup>5</sup> particles μL <sup>-1</sup>	229 particles μL <sup>-1</sup>	[211]
6	PPy@Ti <sub>3</sub> C <sub>2</sub> T <sub>x</sub> /PMo12	Osteopontin	Serum	EIS	–	0.98 fg mL <sup>-1</sup>	[212]
7	AuNPs/Ti <sub>3</sub> C <sub>2</sub> MXene	miRNA-155		EIS, CV	1.0 fM to 10 nM	0.35 fg	[217]
8	MXenes-Apt2/exosomes/Apt1/PNIPAM-AuNPs/GCE	Exosomes, CD63	Serum	ECL	5.0 × 10 <sup>2</sup> to 5.0 × 10 <sup>6</sup> particles μL <sup>-1</sup>	125 particles μL <sup>-1</sup>	[218]
9	MXene-MoS <sub>2</sub> -Thi-AuNPs/GCE	miRNA-21	Serum	CV, EIS, SWV	–	26 fM	[219]
10	CoFe <sub>2</sub> O <sub>4</sub> @Ag-HB5 cytosensor	HER2 positive cells	Blood sample	CV, EIS	10 <sup>2</sup> to 10 <sup>6</sup> cells mL <sup>-1</sup>	47 cells mL <sup>-1</sup>	[220]
11	eCoCu-ZIF@CD-based cytosensor	PTK7B16-F10 cells		EIS, CV	1.0 × 10 <sup>2</sup> to 1.0 × 10 <sup>5</sup> cells mL <sup>-1</sup>	33 cells mL <sup>-1</sup>	[221]

utilized to detect MUC1 through a competitive process that occurs between the cDNA-ferrocene/MXene probe and MUC1. The reduction in an electrical signal happens due to the detachment of the cDNA-Fc/MXene probe from the sensing electrode. This aptasensor has a broad linear range of 1.0–10 μM and a LOD of 0.33 pM, making it suitable for clinical diagnostics [209]. An electrochemiluminescent (ECL) aptasensor for detection of exosomes in breast cancer cells is described by Qiao et al. ECL emitters and reactants used in this study were H<sub>2</sub>O<sub>2</sub> and mercaptopropionic acid (MPA)-modified Eu<sup>3+</sup>-doped CdS nanocrystals (MPA-CdS:Eu NCs), respectively. The CD63 aptamer recognizes and captures exosomes, which subsequently create a G-quadruplex/hemin DNAzyme that competently causes the breakdown of H<sub>2</sub>O<sub>2</sub>, and thereby reduced the ECL signal in MPA-CdS:Eu NCs. The exosomes from breast cancer cells (MCF-7 cells) can be found in concentrations ranging from 3.4 × 10<sup>5</sup> to 1.7 × 10<sup>8</sup> particles mL<sup>-1</sup>. The LOD and signal-to-noise ratio was determined to be

7.41 × 10<sup>4</sup> particles mL<sup>-1</sup>. Exosomes in the serum have been effectively detected using this aptasensors [210]. In a similar study, CD63 aptamer-modified poly(amidoamine) (PAMAM)-Au NP electrode interface which has a high binding affinity for CD63 protein on exosomes generated from OVCAR cells has been fabricated for detection of exosomes. Furthermore, the CD63-modified Ti<sub>3</sub>C<sub>2</sub> MXene was employed as a nanocarrier for several aptamers and was adsorbed to exosomes. The Ti<sub>3</sub>C<sub>2</sub> MXene is generated in situ and loads it efficiently, as well as magnifies the electrochemical signal at a low potential, minimizing interference from the electrochemically active species. This aptasensor shows a linear range of 5 × 10<sup>2</sup> particles μL<sup>-1</sup> to 5 × 10<sup>5</sup> particles μL<sup>-1</sup>, and the LOD was 229 particles μL<sup>-1</sup>. This electrochemical aptasensor can detect exosomes from a variety of cancer cells, including OVCAR, HeLa, and BT474, and in serum samples with high specificity suggesting its clinical diagnostic potential early cancer detection [211]. The nano-hybrid of Ti<sub>3</sub>C<sub>2</sub>T<sub>x</sub> MXene and phosphomolybdic acid



(PMo12) embedded with polypyrrole (denoted as PPy@Ti<sub>3</sub>C<sub>2</sub>T<sub>x</sub>/PMo12) was synthesized by Zhou et al. Further it was attached to osteopontin (OPN) aptamer to build an impedimetric aptasensor for the detection of osteopontin. The fabricated sensor PPy@Ti<sub>3</sub>C<sub>2</sub>T<sub>x</sub>/PMo12 hybrid is endowed with outstanding stability, great biocompatibility, and a significant binding affinity for OPN aptamer. Thus, compared to previously developed bicomponent aptasensors, the PPy@Ti<sub>3</sub>C<sub>2</sub>T<sub>x</sub>/PMo12 hybrid demonstrated improved electrochemical sensing. The aptasensor based on PPy@Ti<sub>3</sub>C<sub>2</sub>T<sub>x</sub>/PMo12 had a detection limit of 0.98 fg mL<sup>-1</sup>, as well as high selectivity and stability, better repeatability, reasonable regenerability, and can be used to detect OPN in human serum samples [212]. The direct laser patterning of various coplanar of MXene on the paper device and multiple devices with series and parallel connections can be fabricated using hydrofluoric acid (HF)-etched and clay-like Ti<sub>3</sub>C<sub>2</sub> MXene slurries in just 17 s using additive manufacturing technique (Fig. 9a) [213]. The fabrication steps of on-chip MXene solid-state micro-supercapacitors (MSCs) by employing a spray-coating method for deposition of highly

conductive Ti<sub>3</sub>C<sub>2</sub>T<sub>x</sub> (L-Ti<sub>3</sub>C<sub>2</sub>T<sub>x</sub>) flakes on a glass substrate were demonstrated by Peng et al. (Fig. 9b). MXene-based composite meets the requirement of the bandgap value which should be between 1.55 and 3.0 eV (Fig. 9c) [214]. They used four steps which include spray coating of small-size Ti<sub>3</sub>C<sub>2</sub>T<sub>x</sub> flakes (s-Ti<sub>3</sub>C<sub>2</sub>T<sub>x</sub>) on top as an electroactive layer, interdigital pattern carved by direct laser cutting of a specific center area (8 × 6 mm<sup>2</sup>) on the stacked MXene film, and a PVA/H<sub>2</sub>SO<sub>4</sub> gel electrolyte was carefully dropped onto the interdigital pattern area, respectively [215]. Employing this process would enable the sensor fabrication with ease and in a cost-effective manner. Fang et al. used black phosphorous quantum dots (BPQDs) and MXenes as a signal amplifier for fabrication of ECL and photothermal dual-mode aptasensor for detection of the cancer-associated exosome. Herein, BPQDs catalyze the oxidation of Ru(dcbpy)<sub>3</sub><sup>2+</sup> and be utilized as a co-reactant. The self-enhanced Ru(dcbpy)<sub>3</sub><sup>2+</sup>@BPQDs ECL system generates a strong ECL signal by shortening electron transfer distance and minimizing energy loss. MXenes provide large specific surface area and excellent conductivity and act as a

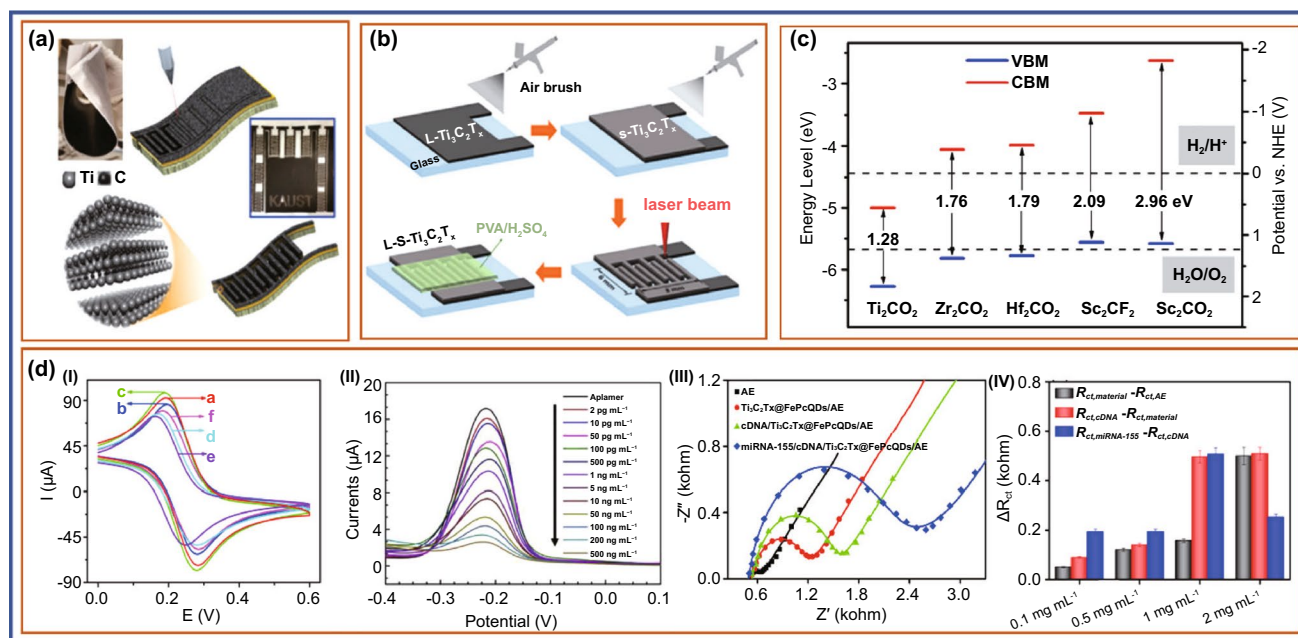


**Fig. 9** **a** Representation of the laser patterning of paper coated with MXene to form an interdigitated electrode for MSCs devices. Copyright from Ref. [213]. **b** Schematic illustrating the fabrication process of the all-Ti<sub>3</sub>C<sub>2</sub>T<sub>x</sub> MXene MSC. Copyright from Ref. [215]. **c** The electronic band-gap for various MXenes sheets. Copyright from Ref. [214]. **d** **(I)** CV curves of different modified electrodes. Copyright from Ref. [166], **(II)** DPV responses to different concentrations (2 to 500 pg mL<sup>-1</sup>) of CEA antigens. Copyright from Ref. [216], **(III)** EIS Nyquist plots of the miRNA-155 detection in 5.0 mM [Fe(CN)<sub>6</sub>]<sup>3-/4-</sup> containing 0.01 M PBS. Copyright from Ref. [167]. **(IV)** The corresponding variations of the R<sub>ct</sub> values with different concentrations (0.1, 0.5, 1, and 2 mg mL<sup>-1</sup>) for detecting miRNA-155 detection procedures (n = 3). Copyright from Ref. [167]

supporter to enhance the number of  $\text{Ru}(\text{dcbpy})_3^{2+}$  and BPQDs immobilized, which improved the ECL signal. They studied the cyclic voltammetry (CV) behaviors of ECL biosensor over electrodes in 5 mM  $[\text{Fe}(\text{CN})_6]^{3-/4-}$  including 0.1 M KCl. As shown in Fig. 9d(I), bare GCE displayed a pair of well-defined redox peak currents (curve a); however, when  $\text{SiO}_2$  nano urchins (NUs) were placed over the electrode, the redox peak current diminished (curve b), which was linked to  $\text{SiO}_2$  NUs with weak conductivity and hence blocking electron transport. The redox peak currents dramatically increased when ILs were coated onto the electrode due to the promotion impact of ILs for electronic transmission (curve c). The redox peak currents reduced dramatically (curve d) after Apt was incubated on the electrode, which was attributed to the aptamer with negatively charged phosphate backbone inhibiting the diffusion of the redox probe  $[\text{Fe}(\text{CN})_6]^{3-/4-}$  to the electrode surface. In exosomes modified electrodes, the redox peak currents are reduced much further (curve e). In contrast to (curve f), when MXenes-BPQDs@ $\text{Ru}(\text{dcbpy})_3^{2+}$ -PEI-AbCD63 (curve f) was deposited onto the electrode, the redox peak currents increased dramatically, indicating that MXenes and BPQDs have a synergistic promotion effect for electron transfer (Fig. 9d(I)). Additionally, both BPQDs and MXenes have a good photothermal effect, which was deftly exploited as athermal converter device in the development of a photothermal biosensor for exosome characterization. The developed dual-modality MXenes-BPQDs probe aptasensor in this study not only enhanced the signal while detection but also provided an effective and reliable approach for exosome detection in cancer patients [166]. A label-free, ultrasensitive, and multiplexed microfluidic paper-based electrochemical aptasensor for simultaneous detection of carcinoembryonic antigen (CEA) and neuron-specific enolase (NSE) was developed by Wang et al. which shows LOD  $2 \text{ pg mL}^{-1}$  for CEA and  $10 \text{ pg mL}^{-1}$  for NSE. The degree of decreased peak currents in DPV responses, which was attributable to the formation of aptamer antigen complex on the electrode surface, was used to detect the two analytes. The currents steadily reduced when CEA (3 A) and NSE increased, as shown in Fig. 9d(II). In the ranges of  $0.01 \sim 500 \text{ ng mL}^{-1}$  for CEA ( $R^2 = 0.989$ ) and  $0.05 \sim 500 \text{ ng mL}^{-1}$  for NSE ( $R^2 = 0.944$ ), the calibration plots revealed a satisfactory linear detection relationship between peak currents and analyte concentrations [216]. Recently, iron phthalocyanine quantum dots (FePcQDs) decorated MXene nanosheets (denoted

as  $\text{Ti}_3\text{C}_2\text{T}_x$ @FePcQDs) and employed as promising nanocarrier of complementary DNA (cDNA) toward miRNA-155. This construct was used as a novel ultrasensitive impedimetric autosensing system for the detection of microRNA-155 (miRNA-155). The  $\text{Ti}_3\text{C}_2\text{T}_x$ @FePcQDs-based aptasensor demonstrated ultrahigh sensitivity with LOD (limit of detection) of  $4.3 \text{ aM}$  ( $S/N = 3$ ) within the miRNA-155 concentration range of  $0.01 \text{ fM}$  to  $10 \text{ pM}$ . for miRNA-155 detection; the suggested impedimetric autosensing system outperformed other published miRNA-155 aptasensors in terms of ease of fabrication, lack of labels, fast reaction time, and better sensing performance for detecting miRNA-155. This technique for determining cancer-associated miRNAs holds a lot of potential for early cancer biomarker detection [166]. Electrochemical impedance spectroscopy (EIS) Nyquist plots of miRNA-155 detection techniques employing an electrochemical aptasensor based on a  $\text{Ti}_3\text{C}_2\text{T}_x$ @FePcQDs nanohybrid in  $5.0 \text{ mM}$   $[\text{Fe}(\text{CN})_6]^{3-/4-}$  in  $0.01 \text{ M}$  PBS are shown in Fig. 9d(III) [167]. The experimental parameters specifically the use of  $\text{Ti}_3\text{C}_2\text{T}_x$ @FePcQD nanohybrid, cDNA concentration, and miRNA-155 binding time onto the  $\text{Ti}_3\text{C}_2\text{T}_x$ @FePcQDs-based aptasensor were tuned to produce excellent sensing performance for miRNA-155 detection. EIS was used for the entire fabrication and detecting process. The  $R_{ct}$  values generated by each step for miRNA-155 detection ( $\text{fM}$ ) utilizing aptasensors based on the  $\text{Ti}_3\text{C}_2\text{T}_x$ @FePcQD nanohybrid with varied usages ( $0.1, 0.5, 1.0, \text{ and } 2.0 \text{ mg mL}^{-1}$ ) under the same conditions are shown in Fig. 9d(IV). The results showed that as the concentration of the  $\text{Ti}_3\text{C}_2\text{T}_x$ @FePcQDs dispersion grew from  $0.1$  to  $1 \text{ mg mL}^{-1}$ , the  $R_{ct}$  values originating from the detection of miRNA-155 increased. When the  $\text{Ti}_3\text{C}_2\text{T}_x$ @FePcQDs dispersion concentration was more than  $1 \text{ mg mL}^{-1}$ , the  $R_{ct}$  value for detecting miRNA-155 dropped dramatically [167].

An electrochemical aptasensor employing an AuNPs/ $\text{Ti}_3\text{C}_2$  nanocomposite for sensitive detection of miRNA-155 using Exonuclease III (Exo III)-assisted cascade has been developed by Yang et al. AuNPs utilize AuS chemical bonds to immobilize capture DNA (C-DNA) on which methylene blue (MB) was tagged at the 3' end of the C-DNA. MiRNA-155 double-stranded structure by complementary base pairing with C-DNA upon which Exo III catalyzes digestion of the double-stranded C-DNA. This led to the electrochemical signal to "switch off." The developed sensor exhibits a linear range of  $1.0 \text{ fM}$  to  $10 \text{ nM}$  and LOD of  $0.35 \text{ fg}$ . ( $S/N = 3$ ). In addition, the developed sensor has

good stability, repeatability, and specificity [217]. Owing to the MXenes properties such as large surface area, excellent conductivity, and catalytic properties, Zhang et al. developed sensitive electrogenerated chemiluminescence (ECL) biosensor for the detection of the exosome. They used aptamer-modified 2D  $\text{Ti}_3\text{C}_2$  MXenes nanosheets as the ECL nanoprobe. An aptamer against EpCAM protein was modified on the surface of the electrode for the capture of the exosome. This ECL nanoprobe showed much-improved luminol ECL signals. The detection limit of this aptasensor was  $125 \text{ particles L}^{-1}$ , which is more than 100 times lower than the detection limit of a standard ELISA approach. The exosomes in the serum were successfully detected using this ECL biosensor and hence can be implemented in clinical diagnostics [218]. Liu et al. combined a 2D bimetallic CoCu-zeolite imidazole framework (CoCu-ZIF) with 0D  $\text{Ti}_3\text{C}_2\text{T}_x$  MXene-derived carbon dots (CDs) and termed it CoCuZIF@CDs. It showed a unique heterogeneous architecture and possesses a sensitive layer for attachment of B16-F10 cell-targeted aptamer strands, hence detecting B16-F10 cells in the biological sample. The characterization showed that CDs were uniformly embedded into CoCu-ZIF NSs with appropriate stacking interaction. This led to enhanced fluorescence performance of 0D/2D CoCu-ZIF@CD nanohybrids. The developed electrochemical aptasensor can be used for cell imaging and detection of living B16-F10 cells. The CoCu-ZIF@CD-based cytosensor exhibits LOD of  $33 \text{ cells mL}^{-1}$  and linear range of detection from  $1.0 \times 10^2$  to  $1.0 \times 10^5 \text{ cells mL}^{-1}$ . In comparison, the CoCu-ZIF@CD-based cytosensor displayed better performance when compared to CoCu-ZIF and CD-based cytosensors. The cell imaging properties, outstanding selectivity, high stability, and good repeatability of developed CoCu-ZIF@CD-based aptasensor can be exploited for early diagnosis of other analytes too by anchoring other probe molecules, hence expanding its applications in biosensing and biomedical domains [66]. A label-free determination of microRNA-21 (miR-21) was successfully demonstrated using an MXene-MoS<sub>2</sub> heterostructure-based electrochemical biosensor conjugated with catalytic hairpin assembly (CHA) amplification. The large specific area and better electroconductivity offered by this unique micro-nanoheterostructure enhance the sensing performance. This MXene-MoS<sub>2</sub> heterostructure triggers more target recycling reactions when compared to traditional CHA amplification approaches. Besides, the anchored thionine and gold nanoparticles (AuNPs) over the

surface of MXene-MoS<sub>2</sub> heterostructure further empowered the sensor performance in terms of probe capture fixation and label-free detection of miR-21. In the detection process, several electronegative double-stranded DNA was generated which hindered the electron transfer resulting in a decrease of a signal. This sensor showed a broad linear range from 100 fM to 100 nM and LOD of about 26 fM. However, this sensor is stable, reproducible, and selective for miR-21 detection and also provides satisfactory and reproducible results. However, the sensing performance of this aptasensor for the detection of miR-21 is found to be either comparable or lower than previous methods even though it showed a promising performance under clinical conditions [219]. In recent research work, Vajhadin et al. developed an aptasensor for electrochemical detection of tumor cells by using HER-2 biomarker. For the development of an aptasensor, the MXene nanosheets of around 2 nm thickness and 1.5  $\mu\text{m}$  lateral size were fabricated over gold electrodes. An HB5 aptamer that shows high selectivity for HER-2-positive cancer cells was then immobilized on the MXene layers. To minimize biofouling of electrode with blood matrix, CoFe<sub>2</sub>O<sub>4</sub>@Ag magnetic nanohybrids bonded to the HB5 were used for magnetic separation of HER-2-positive cancer cells. The magnetically captured cells formed sandwich-like structures with MXene-functionalized electrodes which effectively blocks electron transfer and allows quantitative cell detection when current signal changes. This label-free MXene-based aptasensor exhibited a wide linear range of  $10^2$ – $10^6 \text{ cells mL}^{-1}$  and a LOD of  $47 \text{ cells mL}^{-1}$ . Additionally, it provides decent sensitivity and selectivity against HER2-positive cells detection in blood samples. Therefore, this CoFe<sub>2</sub>O<sub>4</sub>@Ag magnetic nanohybrids and MXenes-based aptacytosensor hold promise to screen cancer progression cost-effectively [220]. The MXene-based 2D material when used in combination with aptamer as biorecognition element for the fabrication of electrochemical aptasensor has enhanced the sensitivity of detection of cancer-associated biomarkers many folds with a linear range of detection as revealed by several studies discussed in this section. However, this field is still in its nascent stage and needs to be explored further in terms of clinical validation of aptasensors in hospitals. Validation of these aptasensors in large cohorts under clinical settings would have the potential to revolutionize the field of cancer diagnostics and needs further attention. The challenges and future perspectives in this regard are discussed in Sect. 6.

## 6 Current Challenges and Prospects

Since the discovery of MXene in 2011, MXenes are widely used in different fields including diagnostic and therapeutic. Although MXene is used widely, some lacunae need to be fulfilled to harvest its full potential. Although their 70+ MXene are known, the number is growing rapidly. There is the possibility to explore many more compounds which are waiting to be included in the MXene family. The synthesis of new MAX phases and other layered carbide and nitride precursors is a hot research direction. The prediction of the various electronic, magnetic, thermal, and chemical properties to get the tunable size, ordered structures, strong surface terminations, and high yielding is needed. This motive can be achieved using computational strategies which can further increase the feasibility of MXene synthesis. With advanced knowledge, the ion dynamics between the sheets of MXene can be controlled or altered to obtain the desired electronic conductivity of the MXene. This can be utilized to fabricate sensors with higher conductivity and lowest resistance to obtain low LOD. Understanding the electrical properties of the MXene can pave new paths in the research field. Very recently, the ionic gel-based highly durable electronic skins were fabricated utilizing ionic gel and MXenes embedded into the polymer matrix. The electronic skin showed excellent mechanical properties, super adhesion, high sensitivity to strain and pressure and could tolerate harsh environment. Owing to the various excellent properties, the fabricated skin can be applied for the multifunctional sensing purposes [193]. Similarly, for serving the healthcare monitoring purpose, the strain sensor was fabricated. The sensor was based on the carbon nanotubes and MXenes into polydimethylsiloxane matrix. The sensor was found to be highly stable, durable, and moreover washable, and could be used for the real-time monitoring of the electrocardiogram (ECG) and joints movements [39]. These types of wearable sensor need to be explored more and utilized for the healthcare monitoring purposes. The conventional synthetic approach of MXene from the MAX phase includes the use of fluoride-containing compounds. The fluoride-containing compounds pose safety hazards and also limit the yield of MXene as it can alter the synthesis of MXene from the Al-containing MAX phase. The fluoride-free approach using hydrochloric acid was also used for the electrochemical etching of the MXene from the MAX phase,

but the over-etching and scaling up remain the challenge. The search for new etching methods has become a frequent topic of research among scientists working in the area of synthesis, so major developments can be expected soon. The main challenge is to develop a sensitive, easy-to-use, cost-effective Point-of-Care-Test (POCT) to eradicate the false-negative and false-positive results.

Certain points limit the use of MXene practically. Firstly, strong acids are used for the exfoliation as the MAX phase layers have strong interactions. The use of these strong acids restricts the use of MXenes in various fields, especially in green chemistry. The other harsh chemicals and use of sophisticated instruments for the synthesis are also a limiting point. This point raises the demand for the new etching methods and experimental conditions which use alternative chemicals. Despite the excellent features, several issues limit the practical applications of MXenes. The majority of the problems arise due to the synthesis process that requires the use of toxic chemicals and harsh experimental conditions. Hence, new experimental routes and conditions should be explored to synthesize novel MXenes with unique properties. In this regard, recently MXene quantum dots were synthesized using watermelon peel extract. The synthesized material was utilized for the biocompatible sensing purposes and also integrated with the smart phone. The more similar work in this field is expected in future for the sensing of various analytes and fabrication of wearable sensor [51]. The use of M in the MAX phase is only limited to some elements Ti, V, Nb, Mo, Ta, Hf. However, many more elements can be used as M in MAX which needs to explore. Instead of metal carbides, metal nitrides can also be used. Till now, there are no more studies available on the different morphology of the MXenes; only the sheet is broadly studied even though other morphology like tube spheres also exists. The complex structure of MXenes during synthesis is still a challenge for researchers [221]. For understanding MXene better, due to its multivariate structure, further studies are needed. Computational approaches can pave the way for designing new MXenes structures. MXenes family can be further expanded by designing and discovering new heterostructures. The search for new etching methods has become a frequent topic of research among scientists working in the area of synthesis, so major developments can be expected soon. The various work has been already done on the MXenes, but still, there is a long way to go. Researchers are working on the greener



synthesis of MXenes for replacing the harsh chemical. By exploring the various properties of MXenes like superconductivity, thermal transport, biocompatibility, etc., it can be exploited to the various multidisciplinary fields. The MXenes displayed tunable magnetic and electric properties and used as an excellent modifier in electrochemical studies and hence showed adaptable applications in various fields such as energy storage, nanomedicine, diagnosis [198]. MXene-enabled aptasensors have shown considerable promise for the early detection of cancer biomarkers. Aptamers have gained much attention in the last few decades and are explored for diagnostic and even therapeutic purposes. The ease of synthesis, low cost, and stability, make aptamer preferable candidate over other BREs. Aptamers also have many pitfalls including difficult multianalyte detection, cross-reactivity, poor precision, etc. The limiting factor in the designing of aptamers is the library design. It usually depends on the oligonucleotide's quality and length, its structural stability, specific binding sequences. The quality of the oligonucleotides depends on the nucleotide's ratio and the level of complexity of an aptamer library. More and more research in the field to make aptamer preferable, cost-effective has improved its demand. More research is in demand for better integration and detection of cancer biomarkers. Advanced bioinformatics techniques and genetic algorithm-based methods are required for studying multiple cancer cells and studying the binding affinities of biomarkers with specific aptamers. Major challenges which need to be addressed include the methods to screen aptamer rapidly with high specificity, maintaining stability in the biological environment, reducing the toxicity of nanomaterials used in conjugation with aptamers. The MXene and aptamer-based devices can be commercialized as POCT devices. Current approaches for the diagnosis of various diseases have been using a lateral flow-based system either in the form of electrical or optical-based devices. The major challenge is device miniaturizations and multiplexing. POCT devices should be affordable, sensitive, specific, user-friendly, robust and can always be performed outside a laboratory or hospital by a non-technical person or by a layman as per ASSURED criteria. Other than cost-cutting, the POC test devices should give a signal in a lesser sample volume (microliter). The device that can differentiate between different biomolecules and can be used for multiplex analyte sensing is the need of the hour. MXene enabled electrochemical aptasensors to have the potential to fulfill the criteria for effective POCT devices for early disease diagnostic.

There is an enormous interest in AI-integrated POCT devices to improve treatment efficacy and health care. A convolutional neural network (CNN) is one of the important AI-based tools that can be integrated with devices for the prediction of disease in resource-limited settings. These devices can also be interlinked with the top-class portable healthcare interfaces such as smartphones, smartwatches, and other wearable devices. These devices can also be used to monitor the healthy as well as the patient's conditions. By integrating these devices with the IoT and IoMT devices, the past and present records of the individual's health condition can be assessed by medical practitioners for better disease prognosis and decision making [222, 223]. These devices can be used to forecast clinical conditions digitally. This will be a rapid, cost-effective, intelligent approach to deal with the disease condition even in resource-limited settings. The detailed insight of MXene-enabled healthcare diagnostics coupled with IoT and IoMT and smartphones and their futuristic application are illustrated in Fig. 10. With the interdisciplinary amalgamation of various fields such as material chemistry, biomedical engineering, computational chemistry, the MXene enabled electrochemical aptasensor to have the potential to tackle the challenges associated with the fabrication and development of POCT devices for early cancer diagnostics.

## 7 Concluding Remarks

Despite the various advancements in the field of oncology, cancer still poses an enormous risk and challenges to tackle. There are several challenging factors which are needed to be addressed and resolved. This review emphasizes of MXene, MXene-based materials, and their conjugation with aptamers for the fabrication of electrochemical aptasensor for cancer diagnostics with a focus on the current trends, important hurdles, and their future insights. The role of nanotechnology in dealing with deadly diseases such as cancer is important. Many portable biomedical devices for imagining, sensing, and other purposes were successfully developed using nanomaterials. MXene is a new class of nanomaterial emerging at a high rate. MXene is significantly used for diagnostic and other biomedical purposes. Many advancements have been made globally by many investigators to explore the properties of MXene. On the other hand, aptasensors as POCT have achieved significant attention in the past few

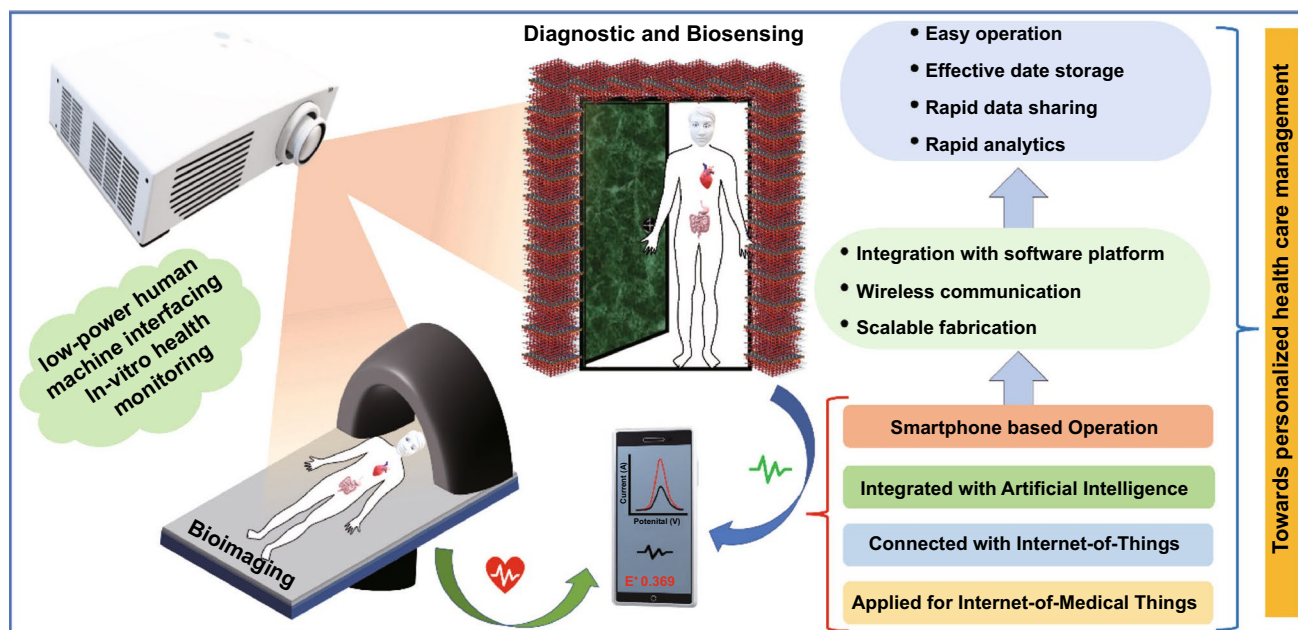


**Fig. 10** Futuristic application of MXene toward personalized healthcare management

decades. The aptamers have remarkable advantages over the conventional biorecognition elements. The aptasensors are economical, stable, sensitive, selective, and show negligible batch-to-batch variation. This review focused on MXene-enabled electrochemical aptasensors for the detection of cancer biomarkers. However, the validation of these aptasensors in a larger patient cohort using a real sample is still needed. Further, challenges associated with device miniaturization, multiplexing, and its integration with IoT-enabled smartphones need to be resolved by using an amalgamation of interdisciplinary fields to optimize the POCT sensing systems. The development of MXene-enabled electrochemical aptasensor for the real-time, cost-effective, and early diagnosis of cancer still has a long way to go. Nevertheless, there are many hurdles in the commercial utilization of the MXene-based aptasensors; however, further research in this field will prepare the base for the commercialization of the MXene-based aptasensors for cancer diagnostics.

**Acknowledgements** The authors express their sincere thanks to Director, CSIR-AMPRI, for his support and encouragement in this work. RK would like to acknowledge SERB for providing funds in the form of the IPA/2020/000130 project. The fellowship provided by DST under the DST-WOS-B scheme to AP is duly acknowledged.

**Funding** Open access funding provided by Shanghai Jiao Tong University.

**Open Access** This article is licensed under a Creative Commons Attribution 4.0 International License, which permits use, sharing, adaptation, distribution and reproduction in any medium or format, as long as you give appropriate credit to the original author(s) and the source, provide a link to the Creative Commons licence, and indicate if changes were made. The images or other third party material in this article are included in the article's Creative Commons licence, unless indicated otherwise in a credit line to the material. If material is not included in the article's Creative Commons licence and your intended use is not permitted by statutory regulation or exceeds the permitted use, you will need to obtain permission directly from the copyright holder. To view a copy of this licence, visit <http://creativecommons.org/licenses/by/4.0/>.

## References

1. H. Sung, J. Ferlay, R.L. Siegel, M. Laversanne, I. Soerjomataram et al., Global cancer statistics 2020: GLOBOCAN estimates of incidence and mortality worldwide for 36 cancers in 185 countries. *CA Cancer J. Clin.* **71**(3), 209–249 (2021). <https://doi.org/10.3322/CAAC.21660>
2. GLOBOCAN 2020: new global cancer data. (UICC, 2020). <https://www.uicc.org/news/globocan-2020-new-global-cancer-data> (Accessed Mar 9, 2022)
3. J. Brodersen, L.M. Schwartz, S. Woloshin, Overdiagnosis: how cancer screening can turn indolent pathology into illness.

- APMIS **122**(8), 683–689 (2014). <https://doi.org/10.1111/APM.12278>
4. N. Goossens, S. Nakagawa, X. Sun, Y. Hoshida, Cancer biomarker discovery and validation. *Transl. Cancer Res.* **4**(3), 256 (2015). <https://doi.org/10.3978/J.ISSN.2218-676X.2015.06.04>
  5. P.R. Srinivas, B.S. Kramer, S. Srivastava, Trends in biomarker research for cancer detection. *Lancet Oncol.* **2**(11), 698–704 (2001). [https://doi.org/10.1016/S1470-2045\(01\)00560-5](https://doi.org/10.1016/S1470-2045(01)00560-5)
  6. R. Khan, A. Parihar, S.K. Sanghi, *Biosensor Based Advanced Cancer Diagnostics: From Lab to Clinics* (ScienceDirect, 2021). <https://doi.org/10.1016/C2020-0-00363-4>
  7. R. Etzioni, N. Urban, S. Ramsey, M. McIntosh, S. Schwartz et al., The case for early detection. *Nat. Rev. Cancer.* **3**(4), 243–252 (2003). <https://doi.org/10.1038/nrc1041>
  8. G.P. Hemstreet, S. Yin, Z. Ma, R.B. Bonner, W. Bi et al., Biomarker risk assessment and bladder cancer detection in a cohort exposed to benzidine. *J. Natl. Cancer Inst.* **93**(6), 427–436 (2001). <https://doi.org/10.1093/JNCI/93.6.427>
  9. H. Kobayashi, H. Sugimoto, S. Onishi, K. Nakano, Novel biomarker candidates for the diagnosis of ovarian clear cell carcinoma (review). *Oncol. Lett.* **10**(2), 612–618 (2015). <https://doi.org/10.3892/ol.2015.3367>
  10. R. Liu, X. Chen, Y. Du, W. Yao, L. Shen et al., Serum micro-RNA expression profile as a biomarker in the diagnosis and prognosis of pancreatic cancer. *Clin. Chem.* **58**(3), 610–618 (2012). <https://doi.org/10.1373/CLINCHEM.2011.172767>
  11. D. Sin, C.M. Tammemagi, S. Lam, M.J. Barnett, X. Duan et al., Pro-surfactant protein B as a biomarker for lung cancer prediction. *J. Clin. Oncol.* **31**(36), 4536 (2013). <https://doi.org/10.1200/JCO.2013.50.6105>
  12. R.M. Witteles, Biomarkers as predictors of cardiac toxicity from targeted cancer therapies. *J. Card. Fail.* **22**(6), 459–464 (2016). <https://doi.org/10.1016/J.CARDFAIL.2016.03.016>
  13. Y. Chen, K. Li, D. Gong, J. Zhang, Q. Li et al., ACLY: a biomarker of recurrence in breast cancer. *Pathol. Res. Pract.* **216**(9), 153076 (2020). <https://doi.org/10.1016/J.PRP.2020.153076>
  14. A. Parihar, S. Jain, D.S. Parihar, P. Ranjan, R. Khan, Biomarkers associated with different types of cancer as a potential candidate for early diagnosis of oncological disorders. *Biosensor Based Advanced Cancer Diagnostics: From Lab to Clinics* 47–57 (2022). <https://doi.org/10.1016/b978-0-12-823424-2.00007-7>
  15. A. Parihar, S. Malviya, R. Khan, Identification of biomarkers associated with cancer using integrated bioinformatic analysis. *Cancer Bioinformatics* (2021). <https://doi.org/10.5772/INTECHOPEN.101432>
  16. A. Parihar, P. Ranjan, S.K. Sanghi, A.K. Srivastava, R. Khan, Point-of-care biosensor-based diagnosis of COVID-19 holds promise to combat current and future pandemics. *ACS Appl. Bio Mater.* **3**(11), 7326–7343 (2020). <https://doi.org/10.1021/acsabm.0c01083>
  17. M. Blanco-Formoso, R.A. Alvarez-Puebla, Cancer diagnosis through SERS and other related techniques. *Int. J. Mol. Sci.* **21**(6), 2253 (2020). <https://doi.org/10.3390/IJMS21062253>
  18. P.S. Bernard, C.T. Wittwer, Real-time PCR technology for cancer diagnostics. *Clin. Chem.* **48**(8), 1178–1185 (2002). <https://doi.org/10.1093/CLINCHEM/48.8.1178>
  19. S. Yadav, M.A. Sadique, P. Ranjan, N. Kumar, A. Singhal et al., SERS based lateral flow immunoassay for point-of-care detection of Sars-Cov-2 in clinical samples. *ACS Appl. Bio Mater.* **4**(4), 2974–2995 (2021). <https://doi.org/10.1021/acsabm.1c00102>
  20. N. Kumar, V.S. Gowri, R. Khan, P. Ranjan, M.A. Sadique et al., Efficiency of nanomaterials for electrochemical diagnostics based point-of-care detection of non-Invasive oral cancer biomarkers. *Adv. Mater. Lett.* **12**(8), 1–20 (2021). <https://doi.org/10.5185/amlett.2021.081651>
  21. P. Ranjan, A. Singhal, S. Yadav, N. Kumar, S. Murali et al., Diagnosis of SARS-CoV-2 using potential point-of-care electrochemical immunosensor: toward the future prospects. *Int. Rev. Immunol.* **40**(1–2), 126–142 (2021). <https://doi.org/10.1080/08830185.2021.1872566>
  22. L.K. Kiiro, D.N. Mbui, P.M. Ntangili, O.J. Onam, F. Oloo, Current biosensors used for early detection of lung cancer biomarkers. *J. Cancer Res. Rev. Rep.* (2021). [https://doi.org/10.47363/JCRR/2021\(3\)148](https://doi.org/10.47363/JCRR/2021(3)148)
  23. P. Ranjan, A. Parihar, S. Jain, N. Kumar, C. Dhand et al., Biosensor-based diagnostic approaches for various cellular biomarkers of breast cancer: a comprehensive review. *Anal. Biochem.* **610**, 113996 (2020). <https://doi.org/10.1016/j.ab.2020.113996>
  24. M. Lakshmanakumar, N. Nesakumar, A.J. Jbb, J.B.B. Rayappan, Electrochemical DNA biosensors for cervical cancers. biomarkers biosens. In *Biomarkers and biosensors for cervical cancer diagnosis: from lab to clinics*, (Springer, Singapore, 2021), pp 57–69. [https://doi.org/10.1007/978-981-16-2586-2\\_5](https://doi.org/10.1007/978-981-16-2586-2_5)
  25. R. Mas-Ballesté, C. Gómez-Navarro, J. Gómez-Herrero, F. Zamora, 2D materials: to graphene and beyond. *Nanoscale* **3**(1), 20–30 (2011). <https://doi.org/10.1039/C0NR00323A>
  26. B. Mortazavi, G. Cuniberti, T. Rabczuk, Mechanical properties and thermal conductivity of graphitic carbon nitride: a molecular dynamics study. *Comput. Mater. Sci.* **99**, 285–289 (2015). <https://doi.org/10.1016/J.COMMATSCI.2014.12.036>
  27. F.A. Rasmussen, K.S. Thygesen, Computational 2D materials database: electronic structure of transition-metal dichalcogenides and oxides. *J. Phys. Chem. C* **119**(23), 13169–13183 (2015). <https://doi.org/10.1021/acs.jpcc.5b02950>
  28. P. Chen, N. Li, X. Chen, W.J. Ong, X. Zhao, The rising star of 2D black phosphorus beyond graphene: synthesis, properties and electronic applications. *2D Mater.* **5**(1), 014002 (2017). <https://doi.org/10.1088/2053-1583/AA8D37>
  29. S. Yadav, M.A. Sadique, A. Kaushik, P. Ranjan, R. Khan et al., Borophene as an emerging 2D flatland for biomedical applications: current challenges and future prospects. *J. Mater. Chem. B* **10**(8), 1146–1175 (2022). <https://doi.org/10.1039/D1TB02277F>
  30. N. Kumar, M.A. Sadique, R. Khan, Electrochemical exfoliation of graphene quantum dots from waste dry cell battery

- for biosensor applications. *Mater. Lett.* **305**, 130829 (2021). <https://doi.org/10.1016/j.matlet.2021.130829>
31. C. Huo, B. Cai, Z. Yuan, B. Ma, H. Zeng et al., Two-dimensional metal halide perovskites: theory, synthesis, and optoelectronics. *Small Methods* **1**(3), 1600018 (2017). <https://doi.org/10.1002/SMTD.201600018>
32. S. Barua, H.S. Dutta, S. Gogoi, R. Devi, R. Khan, Nanostructured MoS<sub>2</sub>-based advanced biosensors: a review. *ACS Appl. Nano Mater.* **1**(1), 2–25 (2017). <https://doi.org/10.1021/ACSANM.7B00157>
33. A. Dhakshinamoorthy, A.M. Asiri, H. Garcia, A. Dhakshinamoorthy, A.M. Asiri et al., 2D metal–organic frameworks as multifunctional materials in heterogeneous catalysis and electro/photocatalysis. *Adv. Mater.* **31**(41), 1900617 (2019). <https://doi.org/10.1002/ADMA.201900617>
34. A. Singhal, A. Parihar, N. Kumar, R. Khan, High throughput molecularly imprinted polymers based electrochemical nanosensors for point-of-care diagnostics of COVID-19. *Mater. Lett.* **306**, 130898 (2022). <https://doi.org/10.1016/j.matlet.2021.130898>
35. J. Yi, J. Li, S. Huang, L. Hu, L. Miao et al., Ti<sub>2</sub>CT<sub>x</sub> MXene-based all-optical modulator. *InfoMat* **2**(3), 601–609 (2020). <https://doi.org/10.1002/inf2.12052>
36. W. Huang, L. Hu, Y. Tang, Z. Xie, H. Zhang et al., Recent advances in functional 2D MXene-based nanostructures for next-generation devices. *Adv. Funct. Mater.* **30**(49), 2005223 (2020). <https://doi.org/10.1002/ADFM.202005223>
37. M. Naguib, M. Kurtoglu, V. Presser, J. Lu, J. Niu et al., Two-dimensional nanocrystals produced by exfoliation of Ti<sub>3</sub>AlC<sub>2</sub>. *Adv. Mater.* **23**(37), 4248–4253 (2011). <https://doi.org/10.1002/ADMA.201102306>
38. X. Li, C. Wang, Y. Cao, G. Wang, Functional MXene materials: progress of their applications. *Chem. An Asian J.* **13**(19), 2742–2757 (2018). <https://doi.org/10.1002/ASIA.201800543>
39. X. Xu, Y. Chen, P. He, S. Wang, K. Ling et al., Wearable CNT/Ti<sub>3</sub>C<sub>2</sub>T<sub>x</sub> MXene/PDMS composite strain sensor with enhanced stability for real-time human healthcare monitoring. *Nano Res.* **14**(8), 2875–2883 (2021). <https://doi.org/10.1007/S12274-021-3536-3>
40. X. Han, J. Huang, H. Lin, Z. Wang, P. Li et al., 2D ultrathin MXene-based drug-delivery nanoplatfor for synergistic photothermal ablation and chemotherapy of cancer. *Adv. Healthc. Mater.* **7**(9), 1701394 (2018). <https://doi.org/10.1002/adhm.201701394>
41. X. Yu, X. Cai, H. Cui, S.W. Lee, X.F. Yu et al., Fluorine-free preparation of titanium carbide MXene quantum dots with high near-infrared photothermal performances for cancer therapy. *Nanoscale* **9**(45), 17859–17864 (2017). <https://doi.org/10.1039/C7NR05997C>
42. C. Zhang, L. Cui, S. Abdolhosseinzadeh, J. Heier, Two-dimensional MXenes for lithium-sulfur batteries. *InfoMat* **2**(4), 613–638 (2020). <https://doi.org/10.1002/inf2.12080>
43. B. Cao, H. Liu, X. Zhang, P. Zhang, Q. Zhu et al., MOF-derived ZnS nanodots/Ti<sub>3</sub>C<sub>2</sub>T<sub>x</sub> MXene hybrids boosting superior lithium storage performance. *Nano-Micro Lett.* **13**, 202 (2021). <https://doi.org/10.1007/S40820-021-00728-X>
44. J. Luo, E. Matios, H. Wang, X. Tao, W. Li, Interfacial structure design of MXene-based nanomaterials for electrochemical energy storage and conversion. *InfoMat* **2**(6), 1057–1076 (2020). <https://doi.org/10.1002/inf2.12118>
45. Z. Ye, Y. Jiang, L. Li, F. Wu, R. Chen, Enhanced catalytic conversion of polysulfide using 1D CoTe and 2D MXene for heat-resistant and lean-electrolyte Li–S batteries. *Chem. Eng. J.* **430**, 132734 (2022). <https://doi.org/10.1016/J.CEJ.2021.132734>
46. A.S. Etman, J. Halim, J. Rosen, Fabrication of Mo1.33CTz(MXene)-cellulose freestanding electrodes for supercapacitor applications. *Mater. Adv.* **2**(2), 743–753 (2021). <https://doi.org/10.1039/d0ma00922a>
47. J. Yin, S. Pan, X. Guo, Y. Gao, D. Zhu et al., Flexible and waterproof 2D/1D/0D construction of MXene-based nanocomposites for electromagnetic wave absorption, EMI shielding, and photothermal conversion. *Nano-Micro Lett.* **13**, 150 (2021). <https://doi.org/10.1007/s40820-021-00673-9>
48. M. Sajid, MXenes: are they emerging materials for analytical chemistry applications?—a review. *Anal. Chim. Acta* **1143**, 267–280 (2021). <https://doi.org/10.1016/J.ACA.2020.08.063>
49. O. Salim, K.A. Mahmoud, K.K. Pant, R.K. Joshi, Introduction to MXenes: synthesis and characteristics. *Mater. Today Chem.* **14**, 100191 (2019). <https://doi.org/10.1016/J.MTCHEM.2019.08.010>
50. K. Maleski, C.E. Ren, M.Q. Zhao, B. Anasori, Y. Gogotsi, Size-dependent physical and electrochemical properties of two-dimensional MXene flakes. *ACS Appl. Mater. Interfaces* **10**(29), 24491–24498 (2018). <https://doi.org/10.1021/ACSAMI.8B04662>
51. J. Sun, H. Du, Z. Chen, L. Wang, G. Shen, MXene quantum dot within natural 3D watermelon peel matrix for biocompatible flexible sensing platform. *Nano Res.* (2021). <https://doi.org/10.1007/S12274-021-3967-X>
52. A. Sundaram, J.S. Ponraj, J.S. Ponraj, C. Wang, W.K. Peng et al., Engineering of 2D transition metal carbides and nitrides MXenes for cancer therapeutics and diagnostics. *J. Mater. Chem. B* **8**(23), 4990–5013 (2020). <https://doi.org/10.1039/D0TB00251H>
53. P. Röthlisberger, M. Hollenstein, Aptamer chemistry. *Adv. Drug Deliv. Rev.* **134**, 3–21 (2018). <https://doi.org/10.1016/J.ADDR.2018.04.007>
54. S. Song, L. Wang, J. Li, C. Fan, J. Zhao, Aptamer-based biosensors. *TrAC. Trends Anal. Chem.* **27**(2), 108–117 (2008). <https://doi.org/10.1016/J.TRAC.2007.12.004>
55. G. Zhou, G. Wilson, L. Hebbard, W. Duan, C. Liddle et al., Aptamers: a promising chemical antibody for cancer therapy. *Oncotarget* **7**(12), 13446 (2016)
56. M. Darmostuk, S. Rimpelova, H. Gbelcova, T. Ruml, Current approaches in SELEX: an update to aptamer selection technology. *Biotechnol. Adv.* **33**(6), 1141–1161 (2015). <https://doi.org/10.1016/J.BIOTECHADV.2015.02.008>
57. P.H.L. Tran, D. Xiang, T.N.G. Nguyen, T.T.D. Tran, Q. Chen et al., Aptamer-guided extracellular vesicle theranostics in oncology. *Theranostics* **10**(9), 3849 (2020). <https://doi.org/10.7150/THNO.39706>



58. B. Guan, X. Zhang, Aptamers as versatile ligands for biomedical and pharmaceutical applications. *Int. J. Nanomed.* **15**, 1059 (2020). <https://doi.org/10.2147/IJN.S237544>
59. R. Savla, O. Taratula, O. Garbuzenko, T. Minko, Tumor targeted quantum dot-mucin I aptamer-doxorubicin conjugate for imaging and treatment of cancer. *J. Control. Release* **153**(1), 16–22 (2011). <https://doi.org/10.1016/J.JCONREL.2011.02.015>
60. M. Sun, S. Liu, X. Wei, S. Wan, M. Huang et al., Aptamer blocking strategy inhibits SARS-CoV-2 virus infection. *Angew. Chem. Int. Ed.* **133**(18), 10354–10360 (2021). <https://doi.org/10.1002/ANGE.202100225>
61. J. Nan, X. Guo, J. Xiao, X. Li, W. Chen et al., Nanoengineering of 2D MXene-based materials for energy storage applications. *Small* **17**(9), 1902085 (2021). <https://doi.org/10.1002/SMLL.201902085>
62. K. Chen, B. Liu, B. Yu, W. Zhong, Y. Lu et al., Advances in the development of aptamer drug conjugates for targeted drug delivery. *WIREs Nanomed. Nanobiotechnol.* **9**(3), e1438 (2017). <https://doi.org/10.1002/WNAN.1438>
63. J.D. Munzar, A. Ng, D. Juncker, Duplexed aptamers: history, design, theory, and application to biosensing. *Chem. Soc. Rev.* **48**(5), 1390–1419 (2019). <https://doi.org/10.1039/C8CS00880A>
64. N. Li, J. Peng, W.J. Ong, T. Ma, Arramel et al., MXenes: an emerging platform for wearable electronics and looking beyond. *Matter* **4**(2), 377–407 (2021). <https://doi.org/10.1016/j.matt.2020.10.024>
65. L. Zhou, F. Wu, J. Yu, Q. Deng, F. Zhang et al., Titanium carbide ( $Ti_3C_2T_x$ ) MXene: a novel precursor to amphiphilic carbide-derived graphene quantum dots for fluorescent ink, light-emitting composite and bioimaging. *Carbon* **118**, 50–57 (2017). <https://doi.org/10.1016/J.CARBON.2017.03.023>
66. G.J. Soufi, P. Iravani, A. Hekmatnia, E. Mostafavi, M. Khatami et al., MXenes and MXene-based materials with cancer diagnostic applications: challenges and opportunities. *Comments Inorg. Chem.* (2021). <https://doi.org/10.1080/02603594.2021.1990890>
67. K. Mao, H. Zhang, Z. Wang, H. Cao, K. Zhang et al., Nano-material-based aptamer sensors for arsenic detection. *Biosens. Bioelectron.* **148**, 111785 (2020). <https://doi.org/10.1016/J.BIOS.2019.111785>
68. Y.W. Cheung, R.M. Dirkwzager, W.C. Wong, J. Cardoso, J.D.N. Costa et al., Aptamer-mediated plasmodium-specific diagnosis of malaria. *Biochimie* **145**, 131–136 (2018). <https://doi.org/10.1016/J.BIOCHI.2017.10.017>
69. C.E. Sunday, M. Chowdhury, Review—aptamer-based electrochemical sensing strategies for breast cancer. *J. Electrochem. Soc.* **168**(2), 027511 (2021). <https://doi.org/10.1149/1945-7111/ABE34D>
70. Q. Wu, G. Chen, S. Qiu, S. Feng, D. Lin, Target-triggered and self-calibration aptasensor based on SERS for precise detection of a prostate cancer biomarker in human blood. *Nanoscale* **13**(16), 7574–7582 (2021). <https://doi.org/10.1039/d1nr00480h>
71. NCI dictionary of cancer terms. <https://www.cancer.gov/publications/dictionaries/cancer-terms> (Accessed Feb 19, 2022)
72. R.M. Califf, Biomarker definitions and their applications. *Exp. Biol. Med.* **243**(3), 213 (2018). <https://doi.org/10.1177/1535370217750088>
73. Diagnostic biomarker. [https://me-pedia.org/wiki/Diagnostic\\_biomarker](https://me-pedia.org/wiki/Diagnostic_biomarker) (Accessed March 03, 2022)
74. I. Martins, I.P. Ribeiro, J. Jorge, A.C. Gonçalves, A.B. Sarmiento-Ribeiro, Liquid biopsies: applications for cancer diagnosis and monitoring. *Genes* **12**(3), 349 (2021). <https://doi.org/10.3390/GENES12030349>
75. BEST (biomarkers, endpoints, and other tools) resource. (NCBI Bookshelf, 2016). <https://www.ncbi.nlm.nih.gov/books/NBK326791> (Accessed Mar 9, 2022)
76. M. Adamaki, V. Zoumpourlis, Prostate cancer biomarkers: from diagnosis to prognosis and precision-guided therapeutics. *Pharmacol. Ther.* **228**, 107932 (2021). <https://doi.org/10.1016/J.PHARMTHERA.2021.107932>
77. H.M. Meng, H. Liu, H. Kuai, R. Peng, L. Mo et al., Aptamer-integrated DNA nanostructures for biosensing, bioimaging and cancer therapy. *Chem. Soc. Rev.* **45**(9), 2583–2602 (2019). <https://doi.org/10.1039/C5CS00645G>
78. M. Jamal-Hanjani, S.A. Quezada, J. Larkin, C. Swanton, Translational implications of tumor heterogeneity. *Clin. Cancer Res.* **21**(6), 1258–1266 (2015). <https://doi.org/10.1158/1078-0432.CCR-14-1429>
79. T. Katsuda, N. Kosaka, T. Ochiya, The roles of extracellular vesicles in cancer biology: toward the development of novel cancer biomarkers. *Proteomics* **14**(4–5), 412–425 (2014). <https://doi.org/10.1002/PMIC.201300389>
80. B. Dai, C. Yin, J. Wu, W. Li, L. Zheng et al., Lab chip a flux-adaptable pump-free microfluidics-based self-contained platform for multiplex cancer biomarker detection. *Lab Chip* **21**(1), 143–153 (2021). <https://doi.org/10.1039/d0lc00944j>
81. L. Wu, X. Qu, Cancer biomarker detection: recent achievements and challenges. *Chem. Soc. Rev.* **44**(10), 2963–2997 (2015). <https://doi.org/10.1039/C4CS00370E>
82. V.S.P.K.S.A. Jayanthi, A.B. Das, U. Saxena, Recent advances in biosensor development for the detection of cancer biomarkers. *Biosens. Bioelectron.* **91**, 15–23 (2017). <https://doi.org/10.1016/j.bios.2016.12.014>
83. J. Zhou, J. Rossi, Aptamers as targeted therapeutics: current potential and challenges. *Nat. Rev. Drug Discov.* **16**(3), 181 (2017). <https://doi.org/10.1038/NRD.2016.199>
84. Y. Morita, M. Leslie, H. Kameyama, D.E. Volk, T. Tanaka, Aptamer therapeutics in cancer: current and future. *Cancers* **10**(3), 80 (2018). <https://doi.org/10.3390/CANCERS10030080>
85. A. Qureshi, I. Roci, Y. Gurbuz, J.H. Niazi, VEGF cancer biomarker protein detection in real human serum using capacitive label-free aptasensor. *Macromol. Symp.* **357**(1), 74–78 (2015). <https://doi.org/10.1002/MASY.201400191>
86. X. Li, X. Ding, J. Fan, Nicking endonuclease-assisted signal amplification of a split molecular aptamer beacon for biomolecule detection using graphene oxide as a sensing platform.

- Analyst **140**(23), 7918–7925 (2015). <https://doi.org/10.1039/C5AN01759A>
87. A. Nabok, H. Abu-Ali, S. Takita, D.P. Smith, Electrochemical detection of prostate cancer biomarker PCA3 using specific RNA-based aptamer labelled with ferrocene. *Chemosensors* **9**(4), 59 (2021). <https://doi.org/10.3390/chemosensors9040059>
88. A. Díaz-Fernández, R. Miranda-Castro, N. de-los-Santos-Álvarez, M.J. Lobo-Castañón, P. Estrela, Impedimetric aptamer-based glycan PSA score for discrimination of prostate cancer from other prostate diseases. *Biosens. Bioelectron.* **175**, 112872 (2021). <https://doi.org/10.1016/j.bios.2020.112872>
89. H. Wan, X. Cao, M. Liu, F. Zhang, C. Sun et al., Aptamer and bifunctional enzyme co-functionalized MOF-derived porous carbon for low-background electrochemical aptasensing. *Anal. Bioanal. Chem.* **413**(25), 6303–6312 (2021). <https://doi.org/10.1007/s00216-021-03585-0>
90. S.R. Nxele, T. Nyokong, The effects of the composition and structure of quantum dots combined with cobalt phthalocyanine and an aptamer on the electrochemical detection of prostate specific antigen. *Dyes Pigments* **192**, 109407 (2021). <https://doi.org/10.1016/j.dyepig.2021.109407>
91. S.S.S. Toloun, L. Pishkar, Study of the prostate-specific antigen–aptamer stability in the PSA–aptamer–single wall carbon nanotube assembly by docking and molecular dynamics simulation. *Mol. Simul.* **47**(12), 951–959 (2021). <https://doi.org/10.1080/08927022.2021.1932874>
92. Y. Wang, X. Kan, Sensitive and selective “signal-off” electrochemiluminescence sensing for prostate-specific antigen based on aptamer and molecularly imprinted polymer. *Analyst* **146**(24), 7693–7701 (2021). <https://doi.org/10.1039/d1an01645h>
93. N. Ma, W. Jiang, T. Li, Z. Zhang, H. Qi et al., Fluorescence aggregation assay for the protein biomarker mucin I using carbon dot-labeled antibodies and aptamers. *Microchim. Acta* **182**(1–2), 443–447 (2015). <https://doi.org/10.1007/s00604-014-1386-3>
94. L. Zhao, M. Cheng, G. Liu, H. Lu, Y. Gao et al., A fluorescent biosensor based on molybdenum disulfide nanosheets and protein aptamer for sensitive detection of carcinoembryonic antigen. *Sens. Actuators B Chem.* **273**, 185–190 (2018). <https://doi.org/10.1016/j.snb.2018.06.004>
95. Y. Wang, L. Chen, T. Xuan, J. Wang, X. Wang, Label-free electrochemical impedance spectroscopy aptasensor for ultrasensitive detection of lung cancer biomarker carcinoembryonic antigen. *Front. Chem.* **9**, 721008 (2021). <https://doi.org/10.3389/fchem.2021.721008>
96. B. Bao, P. Su, J. Zhu, J. Chen, Y. Xu et al., Rapid aptasensor capable of simply detect tumor markers based on conjugated polyelectrolytes. *Talanta* **190**, 204–209 (2018). <https://doi.org/10.1016/j.talanta.2018.07.072>
97. J. Shi, J. Lyu, F. Tian, M. Yang, A fluorescence turn-on biosensor based on graphene quantum dots (GQDs) and molybdenum disulfide (MoS<sub>2</sub>) nanosheets for epithelial cell adhesion molecule (EpCAM) detection. *Biosens. Bioelectron.* **93**, 182–188 (2017). <https://doi.org/10.1016/j.bios.2016.09.012>
98. Y. Wang, S. Sun, J. Luo, Y. Xiong, T. Ming et al., Low sample volume origami-paper-based graphene-modified aptasensors for label-free electrochemical detection of cancer biomarker-EGFR. *Microsyst. Nanoeng.* **6**(1), 32 (2020). <https://doi.org/10.1038/s41378-020-0146-2>
99. Z. Hao, Y. Pan, W. Shao, Q. Lin, X. Zhao, Graphene-based fully integrated portable nanosensing system for on-line detection of cytokine biomarkers in saliva. *Biosens. Bioelectron.* **134**, 16–23 (2019). <https://doi.org/10.1016/j.bios.2019.03.053>
100. K. Zhang, M. Pei, Y. Cheng, Z. Zhang, C. Niu et al., A novel electrochemical aptamer biosensor based on tetrahedral DNA nanostructures and catalytic hairpin assembly for CEA detection. *J. Electroanal. Chem.* **898**, 115635 (2021). <https://doi.org/10.1016/j.jelechem.2021.115635>
101. H. Lee, D.H.M. Dam, J.W. Ha, J. Yue, T.W. Odom, Enhanced human epidermal growth factor receptor 2 degradation in breast cancer cells by lysosome-targeting gold nanoconstructs. *ACS Nano* **9**(10), 9859–9867 (2015). <https://doi.org/10.1021/acs.nano.5b05138>
102. T. Harahsheh, Y.F. Makableh, I. Rawashdeh, M. Al-Fandi, Enhanced aptasensor performance for targeted HER2 breast cancer detection by using screen-printed electrodes modified with Au nanoparticles. *Biomed. Microdevices* **23**(4), 46 (2021). <https://doi.org/10.1007/s10544-021-00586-9>
103. Z. Wang, J. Luo, M. Yang, X. Wang, Photoelectrochemical assay for the detection of circulating tumor cells based on aptamer-Ag<sub>2</sub>S nanocrystals for signal amplification. *Anal. Bioanal. Chem.* **413**(21), 5259–5266 (2021). <https://doi.org/10.1007/s00216-021-03502-5>
104. D.C. Ferreira, M.R. Batistuti, B. Bachour, M. Mulato, Aptasensor based on screen-printed electrode for breast cancer detection in undiluted human serum. *Bioelectrochemistry* **137**, 107586 (2021). <https://doi.org/10.1016/j.bioelechem.2020.107586>
105. M. Loyez, M. Lobry, E.M. Hassan, M.C. DeRosa, C. Caucheteur et al., HER2 breast cancer biomarker detection using a sandwich optical fiber assay. *Talanta* **221**, 121452 (2021). <https://doi.org/10.1016/j.talanta.2020.121452>
106. S. Rauf, A.A. Lahcen, A. Aljedaibi, T. Beduk, J.I.O. Filho et al., Gold nanostructured laser-scribed graphene: a new electrochemical biosensing platform for potential point-of-care testing of disease biomarkers. *Biosens. Bioelectron.* **180**, 113116 (2021). <https://doi.org/10.1016/j.bios.2021.113116>
107. R.M. Eaton, J.A. Shallcross, L.E. Mael, K.S. Mears, L. Minkoff et al., Selection of DNA aptamers for ovarian cancer biomarker HE4 using CE-SELEX and high-throughput sequencing. *Anal. Bioanal. Chem.* **407**(23), 6965–6973 (2015). <https://doi.org/10.1007/s00216-015-8665-7>
108. X. Zhang, Y. Wang, H. Deng, X. Xiong, H. Zhang et al., An aptamer biosensor for CA125 quantification in human serum based on upconversion luminescence resonance energy



- transfer. *Microchem. J.* **161**, 105761 (2021). <https://doi.org/10.1016/j.microc.2020.105761>
109. Z. Hu, X. Zhou, J. Duan, X. Wu, J. Wu et al., Aptamer-based novel Ag-coated magnetic recognition and SERS nanotags with interior nanogap biosensor for ultrasensitive detection of protein biomarker. *Sens. Actuators B Chem.* **334**, 129640 (2021). <https://doi.org/10.1016/j.snb.2021.129640>
110. S. Li, X. Liu, S. Liu, M. Guo, C. Liu et al., Fluorescence sensing strategy based on aptamer recognition and mismatched catalytic hairpin assembly for highly sensitive detection of alpha-fetoprotein. *Anal. Chim. Acta* **1141**, 21 (2021). <https://doi.org/10.1016/j.aca.2020.10.030>
111. R. Gao, C. Zhan, C. Wu, Y. Lu, B. Cao et al., Simultaneous single-cell phenotype analysis of hepatocellular carcinoma CTCs using a SERS-aptamer based microfluidic chip. *Lab Chip* **21**(20), 3888–3898 (2021). <https://doi.org/10.1039/d1lc00516b>
112. Y.C. Tsai, C.S. Lin, C.N. Lin, K.F. Hsu, G.B. Lee, Screening aptamers targeting the cell membranes of clinical cancer tissues on an integrated microfluidic system. *Sens. Actuators B Chem.* **330**, 129334 (2021). <https://doi.org/10.1016/j.snb.2020.129334>
113. M. Liu, L. Xi, T. Tan, L. Jin, Z. Wang et al., Chinese a novel aptamer-based histochemistry assay for specific diagnosis of clinical breast cancer tissues. *Chinese Chem. Lett.* **32**(5), 1726–1730 (2021). <https://doi.org/10.1016/j.ccllet.2020.11.072>
114. C. Zhu, L. Li, S. Fang, Y. Zhao, L. Zhao et al., Selection and characterization of an ssDNA aptamer against thyroglobulin. *Talanta* **223**(P1), 121690 (2021). <https://doi.org/10.1016/j.talanta.2020.121690>
115. A. Miranda, T. Santos, J. Carvalho, D. Alexandre, A. Jardim et al., Aptamer-based approaches to detect nucleolin in prostate cancer. *Talanta* **226**, 122037 (2020). <https://doi.org/10.1016/j.talanta.2020.122037>
116. C.F. Shi, Z.Q. Li, C. Wang, J. Li, X.H. Xia, Ultrasensitive plasmon enhanced Raman scattering detection of nucleolin using nanochannels of 3D hybrid plasmonic metamaterial. *Biosens. Bioelectron.* **178**, 113040 (2021). <https://doi.org/10.1016/j.bios.2021.113040>
117. Z. Li, X. Miao, Z. Cheng, P. Wang, Hybridization chain reaction coupled with the fluorescence quenching of gold nanoparticles for sensitive cancer protein detection. *Sens. Actuators B Chem.* **243**, 731–737 (2017). <https://doi.org/10.1016/j.snb.2016.12.047>
118. M. Asgari, H. Khanahmad, H. Motaghi, A. Farzadnia, M.A. Mehrgardi et al., Aptamer modified nanoprobe for multimodal fluorescence/magnetic resonance imaging of human ovarian cancer cells. *Appl. Phys. A Mater. Sci. Proc.* **127**(1), 47 (2021). <https://doi.org/10.1007/s00339-020-04171-4>
119. S. Takita, A. Nabok, D. Smith, A. Lishchuk, Comparison of the performances of two RNA-based genosensing principles for the detection of LncPCA3 biomarker. *Chem. Proc.* **3**, (2021). <https://sciforum.net/manuscripts/10453/manuscript.pdf>
120. S. Forouzanfar, F. Alam, N. Pala, C. Wang, Highly sensitive label-free electrochemical aptasensors based on photoresist derived carbon for cancer biomarker detection. *Biosens. Bioelectron.* **170**, 112598 (2020). <https://doi.org/10.1016/j.bios.2020.112598>
121. S. Chung, J.K. Sicklick, P. Ray, D.A. Hall, Development of a soluble KIT electrochemical aptasensor for cancer theranostics. *ACS Sens.* **6**(5), 1971–1979 (2021). <https://doi.org/10.1021/acssensors.1c00535>
122. S. Lee, S. Hayati, S. Kim, H.J. Lee, Determination of protein tyrosine kinase-7 concentration using electrocatalytic reaction and an aptamer-antibody sandwich assay platform. *Catal. Today* **359**, 76–82 (2021). <https://doi.org/10.1016/j.cattod.2019.05.029>
123. H. Wang, X. Li, L.A. Lai, T.A. Brentnall, D.W. Dawson et al., X-aptamers targeting Thy-1 membrane glycoprotein in pancreatic ductal adenocarcinoma. *Biochimie* **181**, 25–33 (2021). <https://doi.org/10.1016/j.biochi.2020.11.018>
124. S. Gogoi, R. Khan, Fluorescence immunosensor for cardiac troponin T based on Förster resonance energy transfer (FRET) between carbon dot and MoS<sub>2</sub> nano-couple. *Phys. Chem. Chem. Phys.* **20**(24), 16501–16509 (2018). <https://doi.org/10.1039/C8CP02433B>
125. F. Odeh, H. Nsairat, W. Alshaer, M.A. Ismail, E. Esawi et al., Aptamers chemistry: chemical modifications and conjugation strategies. *Molecules* **25**(1), 3 (2019). <https://doi.org/10.3390/MOLECULES25010003>
126. S. Cai, J. Yan, H. Xiong, Y. Liu, D. Peng et al., Investigations on the interface of nucleic acid aptamers and binding targets. *Analyst* **143**(22), 5317–5338 (2018). <https://doi.org/10.1039/C8AN01467A>
127. B. Chatterjee, N. Kalyani, A. Anand, E. Khan, S. Das et al., GOLD SELEX: a novel SELEX approach for the development of high-affinity aptamers against small molecules without residual activity. *Microchim. Acta* **187**(11), 618 (2020). <https://doi.org/10.1007/S00604-020-04577-0>
128. T. Adachi, Y. Nakamura, Aptamers: a review of their chemical properties and modifications for therapeutic application. *Molecules* **24**(23), 4229 (2019). <https://doi.org/10.3390/MOLECULES24234229>
129. M. Sola, A.P. Menon, B. Moreno, D. Meraviglia-Crivelli, M.M. Soldevilla et al., Aptamers against live targets: is in vivo SELEX finally coming to the edge? *Mol. Ther. Nucleic Acids* **21**, 192–204 (2020). <https://doi.org/10.1016/j.omtn.2020.05.025>
130. A. Parashar, J. Clin, Aptamers in therapeutics. *J. Clin. Diagn. Res.* (2016). <https://doi.org/10.7860/JCDR/2016/18712.7922>
131. A. Brady, H.W. Wang, M. Naguib, K. Liang, V.Q. Vuong et al., Pre-sodiated Ti<sub>3</sub>C<sub>2</sub>T<sub>x</sub> MXene structure and behavior as electrode for sodium-ion capacitors. *ACS Nano* **15**(2), 2994–3003 (2021). <https://doi.org/10.1021/acsnano.0c09301>
132. Á. Morales-García, F. Calle-Vallejo, F. Illas, MXenes: new horizons in catalysis. *ACS Catal.* **10**(22), 13487–13503 (2020). <https://doi.org/10.1021/ACSCATAL.0C03106>

133. K. Maleski, M. Alhabeb, Top-down MXene synthesis (selective etching). *2D Metal Carbides and Nitrides (MXenes)* 69–87 (2019). [https://doi.org/10.1007/978-3-030-19026-2\\_5](https://doi.org/10.1007/978-3-030-19026-2_5)
134. K. Xiong, P. Wang, G. Yang, Z. Liu, H. Zhang et al., Functional group effects on the photoelectronic properties of MXene ( $\text{Sc}_2\text{CT}_2$ , T=O, F, OH) and their possible photocatalytic activities. *Sci. Rep.* **7**(1), 15095 (2017). <https://doi.org/10.1038/s41598-017-15233-8>
135. Y. Jia, Y. Pan, C. Wang, C. Liu, C. Shen et al., Flexible Ag microparticle/MXene-based film for energy harvesting. *Nano-Micro Lett.* **13**, 201 (2021). <https://doi.org/10.1007/S40820-021-00729-W>
136. I. Persson, L.A. Näslund, J. Halim, M.W. Barsoum, V. Darakchieva et al., On the organization and thermal behavior of functional groups on  $\text{Ti}_3\text{C}_2$  surfaces in vacuum. *2D Mater* **5**(1), 015002 (2017). <https://doi.org/10.1088/2053-1583/AA89CD>
137. N.R. Hemanth, B. Kandasubramanian, Recent advances in 2D MXenes for enhanced cation intercalation in energy harvesting applications: a review. *Chem. Eng. J.* **392**, 123678 (2020). <https://doi.org/10.1016/J.CEJ.2019.123678>
138. R. Syamsai, J.R. Rodriguez, V.G. Pol, Q.V. Le, K.M. Bato et al., Double transition metal MXene ( $\text{Ti}_x\text{Ta}_{4-x}\text{C}_3$ ) 2D materials as anodes for Li-ion batteries. *Sci. Rep.* **11**(1), 688 (2021). <https://doi.org/10.1038/s41598-020-79991-8>
139. R.M. Ronchi, J.T. Arantes, S.F. Santos, Synthesis, structure, properties and applications of MXenes: current status and perspectives. *Ceram. Int.* **45**(15), 18167–18188 (2019). <https://doi.org/10.1016/J.CERAMINT.2019.06.114>
140. N. Xu, H. Li, Y. Gan, H. Chen, W. Li et al., Zero-dimensional MXene-based optical devices for ultrafast and ultranarrow photonics applications. *Adv. Sci.* **7**(22), 2002209 (2020). <https://doi.org/10.1002/adv.202002209>
141. F. Wu, Z. Liu, J. Wang, T. Shah, P. Liu et al., Template-free self-assembly of MXene and CoNi-bimetal MOF into intertwined one-dimensional heterostructure and its microwave absorbing properties. *Chem. Eng. J.* **422**, 130591 (2021). <https://doi.org/10.1016/j.cej.2021.130591>
142. X. Zhao, X.J. Zha, J.H. Pu, L. Bai, R.Y. Bao et al., Macroporous three-dimensional MXene architectures for highly efficient solar steam generation. *J. Mater. Chem. A* **7**(17), 10446–10455 (2019). <https://doi.org/10.1039/c9ta00176j>
143. Z. Xiang, Y. Shi, X. Zhu, L. Cai, W. Lu, Flexible and waterproof 2D/1D/0D construction of MXene-based nanocomposites for electromagnetic wave absorption, EMI shielding, and photothermal conversion. *Nano-Micro Lett.* **13**, 150 (2021). <https://doi.org/10.1007/S40820-021-00673-9>
144. D. Wang, L. Wang, Z. Lou, Y. Zheng, K. Wang et al., Biocompatible and robust silk fibroin-MXene film with stable 3D cross-link structure for flexible pressure sensors. *Nano Energy* **78**, 105252 (2020). <https://doi.org/10.1016/J.NANOEN.2020.105252>
145. C.E. Shuck, K. Ventura-Martinez, A. Goad, S. Uzun, M. Shekhirev et al., Safe synthesis of MAX and MXene: guidelines to reduce risk during synthesis. *ACS Chem. Health Saf.* **28**(5), 326–338 (2021). <https://doi.org/10.1021/acs.chas.1c00051>
146. M. Malaki, A. Maleki, R.S. Varma, MXenes and ultrasonication. *J. Mater. Chem. A* **7**(18), 10843–10857 (2019). <https://doi.org/10.1039/C9TA01850F>
147. Z. Ling, C.E. Ren, M.Q. Zhao, J. Yang, J.M. Giammarco et al., Flexible and conductive MXene films and nanocomposites with high capacitance. *PNAS* **111**(47), 16676–16681 (2014). <https://doi.org/10.1073/PNAS.1414215111>
148. R.A. Vaia, A. Jawaid, A. Hassan, G. Neher, D. Nepal et al., Halogen etch of  $\text{Ti}_3\text{AlC}_2$  MAX phase for MXene fabrication. *ACS Nano* **15**(2), 2771–2777 (2021). <https://doi.org/10.1021/ACS.NANO.0C08630>
149. T. Li, L. Yao, Q. Liu, J. Gu, R. Luo et al., Fluorine-free synthesis of high-purity  $\text{Ti}_3\text{C}_2\text{T}_x$  (T=OH, O) via alkali treatment. *Angew. Chem. Int. Ed.* **130**(21), 6223–6227 (2018). <https://doi.org/10.1002/ANGE.201800887>
150. P. Urbankowski, B. Anasori, T. Makaryan, D. Er, S. Kota et al., Synthesis of two-dimensional titanium nitride  $\text{Ti}_4\text{N}_3$  (MXene). *Nanoscale* **8**(22), 11385–11391 (2016). <https://doi.org/10.1039/C6NR02253G>
151. S. Yang, P. Zhang, F. Wang, A.G. Ricciardulli, M.R. Lohe et al., Fluoride-free synthesis of two-dimensional titanium carbide (MXene) using a binary aqueous system. *Angew. Chem. Int. Ed.* **57**(47), 15491–15495 (2018). <https://doi.org/10.1002/ANIE.201809662>
152. C.J. Zhang, S. Pinilla, N. McEvoy, C.P. Cullen, B. Anasori et al., Oxidation stability of colloidal two-dimensional titanium carbides (MXenes). *Chem. Mater.* **29**(11), 4848–4856 (2017). <https://doi.org/10.1021/ACS.CHEMMATER.7B00745>
153. M. Naguib, R.R. Unocic, B.L. Armstrong, J. Nanda, Large-scale delamination of multi-layers transition metal carbides and carbonitrides “MXenes.” *Dalt. Trans.* **44**(20), 9353–9358 (2015). <https://doi.org/10.1039/C5DT01247C>
154. H. Tang, H. Tang, Y. Yang, Y. Yang, R. Wang et al., Improving the properties of 2D titanium carbide films by thermal treatment. *J. Mater. Chem. C* **8**(18), 6214–6220 (2020). <https://doi.org/10.1039/C9TC07018D>
155. J. Ran, G. Gao, F.T. Li, T.Y. Ma, A. Du et al.,  $\text{Ti}_3\text{C}_2$  MXene co-catalyst on metal sulfide photo-absorbers for enhanced visible-light photocatalytic hydrogen production. *Nat. Commun.* **8**, 13907 (2017). <https://doi.org/10.1038/ncomms13907>
156. L. Wang, H. Qiu, P. Song, Y. Zhang, Y. Lu et al., 3D  $\text{Ti}_3\text{C}_2\text{T}_x$  MXene/C hybrid foam/epoxy nanocomposites with superior electromagnetic interference shielding performances and robust mechanical properties. *Compos. Part A Appl. Sci. Manuf.* **123**, 293–300 (2019). <https://doi.org/10.1016/J.COMPOSITESA.2019.05.030>
157. Y. Fang, R. Hu, B. Liu, Y. Zhang, K. Zhu et al., MXene-derived  $\text{TiO}_2$  /reduced graphene oxide composite with an enhanced capacitive capacity for Li-ion and K-ion batteries. *J. Mater. Chem. A* **7**(10), 5363–5372 (2019). <https://doi.org/10.1039/C8TA12069B>
158. A. Sinha, Dhanjai, H. Zhao, Y. Huang, X. Lu et al., MXene: an emerging material for sensing and biosensing. *TrAC Trends Anal. Chem.* **105**, 424–435 (2018). <https://doi.org/10.1016/J.TRAC.2018.05.021>

159. Z. Li, Y. Wu, Z. Li, Y. Wu, 2D early transition metal carbides (MXenes) for catalysis. *Small* **15**(29), 1804736 (2019). <https://doi.org/10.1002/SMLL.201804736>
160. T. Wang, T. Wang, C. Weng, L. Liu, J. Zhao et al., Engineering electrochemical actuators with large bending strain based on 3D-structure titanium carbide MXene composites. *Nano Res.* **14**(7), 2277–2284 (2021). <https://doi.org/10.1007/S12274-020-3222-X>
161. S.J. Kim, H.J. Koh, C.E. Ren, O. Kwon, K. Maleski et al., Metallic  $Ti_3C_2T_x$  MXene gas sensors with ultrahigh signal-to-noise ratio. *ACS Nano* **12**(2), 986–993 (2018). <https://doi.org/10.1021/ACSANO.7B07460>
162. B. Shen, H. Huang, H. Liu, Q. Jiang, H. He, Bottom-up construction of three-dimensional porous MXene/nitrogen-doped graphene architectures as efficient hydrogen evolution electrocatalysts. *Int. J. Hydrogen Energy* **46**(58), 29984–29993 (2021). <https://doi.org/10.1016/J.IJHYDENE.2021.06.157>
163. K. Li, X. Wang, S. Li, P. Urbankowski, J. Li et al., An ultrafast conducting polymer@MXene positive electrode with high volumetric capacitance for advanced asymmetric supercapacitors. *Small* **16**(4), 1906851 (2020). <https://doi.org/10.1002/sml.201906851>
164. A. Lipatov, M. Alhabeab, M.R. Lukatskaya, A. Boson, Y. Gogotsi et al., Effect of synthesis on quality, electronic properties and environmental stability of individual monolayer  $Ti_3C_2$  MXene flakes. *Adv. Electron. Mater.* **2**(12), 1600255 (2016). <https://doi.org/10.1002/aelm.201600255>
165. M. Alhabeab, K. Maleski, B. Anasori, P. Lelyukh, L. Clark et al., Guidelines for synthesis and processing of two-dimensional titanium carbide ( $Ti_3C_2T_x$  MXene). *Chem. Mater.* **29**(18), 7633–7644 (2017). <https://doi.org/10.1021/acs.chemmater.7b02847>
166. D. Fang, D. Zhao, S. Zhang, Y. Huang, H. Dai et al., Black phosphorus quantum dots functionalized MXenes as the enhanced dual-mode probe for exosomes sensing. *Sens. Actuators B Chem.* **305**, 127544 (2020). <https://doi.org/10.1016/J.SNB.2019.127544>
167. F. Duan, C. Guo, M. Hu, Y. Song, M. Wang et al., Construction of the 0D/2D heterojunction of  $Ti_3C_2T_x$  MXene nanosheets and iron phthalocyanine quantum dots for the impedimetric aptasensing of microRNA-155. *Sens. Actuators B Chem.* **310**, 127844 (2020). <https://doi.org/10.1016/J.SNB.2020.127844>
168. B.C. Wyatt, A. Rosenkranz, B. Anasori, B.C. Wyatt, B. Anasori et al., 2D MXenes: tunable mechanical and tribological properties. *Adv. Mater.* **33**(17), 2007973 (2021). <https://doi.org/10.1002/ADMA.202007973>
169. I. Persson, A. Ghazaly, Q. Tao, J. Halim, S. Kota et al., Tailoring structure, composition, and energy storage properties of MXenes from selective etching of in-plane, chemically ordered MAX phases. *Small* **14**(17), 1703676 (2018). <https://doi.org/10.1002/SMLL.201703676>
170. V.N. Borysiuk, V.N. Mochalin, Y. Gogotsi, Bending rigidity of two-dimensional titanium carbide (MXene) nanoribbons: a molecular dynamics study. *Comput. Mater. Sci.* **143**, 418–424 (2018). <https://doi.org/10.1016/J.COMMATSCI.2017.11.028>
171. S.M. Hatam-Lee, A. Esfandiari, A. Rajabpour, Mechanical behaviors of titanium nitride and carbide MXenes: a molecular dynamics study. *Appl. Surf. Sci.* **566**, 150633 (2021). <https://doi.org/10.1016/J.APSUSC.2021.150633>
172. G. Plummer, B. Anasori, Y. Gogotsi, G.J. Tucker, Nanoindentation of monolayer  $Ti_{n+1}C_nT_x$  MXenes via atomistic simulations: the role of composition and defects on strength. *Comput. Mater. Sci.* **157**, 168–174 (2019). <https://doi.org/10.1016/J.COMMATSCI.2018.10.033>
173. K. Ren, R. Zheng, P. Xu, D. Cheng, W. Huo et al., Electronic and optical properties of atomic-scale heterostructure based on MXene and MN (M = Al, Ga): a DFT investigation. *Nanomaterials* **11**(9), 2236 (2021). <https://doi.org/10.3390/NANO11092236>
174. K. Hantanasirisakul, M.Q. Zhao, P. Urbankowski, J. Halim, B. Anasori et al., Fabrication of  $Ti_3C_2T_x$  MXene transparent thin films with tunable optoelectronic properties. *Adv. Electron. Mater.* **2**(6), 1600050 (2016). <https://doi.org/10.1002/AELM.201600050>
175. Y. Xu, Y. Wang, J. An, A.C. Sedgwick, M. Li et al., 2D-ultrathin MXene/DOXjade platform for iron chelation chemo-photothermal therapy. *Bioact. Mater.* **14**, 76–85 (2021). <https://doi.org/10.1016/J.BIOACTMAT.2021.12.011>
176. C.J. Zhang, B. Anasori, A. Seral-Ascaso, S.H. Park, N. McEvoy et al., Transparent, flexible, and conductive 2D titanium carbide (MXene) films with high volumetric capacitance. *Adv. Mater.* **29**(36), 1702678 (2017). <https://doi.org/10.1002/ADMA.201702678>
177. C. Xing, S. Chen, X. Liang, Q. Liu, M. Qu et al., Two-dimensional MXene ( $Ti_3C_2$ )-integrated cellulose hydrogels: toward smart three-dimensional network nanoplatforms exhibiting light-induced swelling and bimodal photothermal/chemotherapy anticancer activity. *ACS Appl. Mater. Interfaces* **10**(33), 27631–27643 (2018). <https://doi.org/10.1021/ACSAMI.8B08314>
178. G. Ying, S. Kota, A.D. Dillon, A.T. Fafarman, M.W. Barsoum, Conductive transparent  $V_2CT_x$  (MXene) films. *FlatChem* **8**, 25–30 (2018). <https://doi.org/10.1016/J.FLATC.2018.03.001>
179. G.R. Berdiyrov, Optical properties of functionalized  $Ti_3C_2T_2$  (T = F, O, OH) MXene: first-principles calculations. *AIP Adv.* **6**(5), 055105 (2016). <https://doi.org/10.1063/1.4948799>
180. J. Wang, X. Zhou, M. Yang, D. Cao, X. Chen et al., Interface and polarization effects induced Schottky-barrier-free contacts in two-dimensional MXene/GaN heterojunctions. *J. Mater. Chem. C* **8**(22), 7350–7357 (2020). <https://doi.org/10.1039/D0TC01405B>
181. R. Li, L. Zhang, L. Shi, P. Wang, MXene  $Ti_3C_2$ : an effective 2D light-to-heat conversion material. *ACS Nano* **11**(4), 3752–3759 (2017). <https://doi.org/10.1021/ACSANO.6B08415>
182. Z. Huang, X. Cui, S. Li, J. Wei, P. Li et al., Two-dimensional MXene-based materials for photothermal therapy. *Nanophotonics* **9**(8), 2233–2249 (2020). <https://doi.org/10.1515/nanoph-2019-0571>
183. A. Paściak, A. Pilch-Wróbel, Ł. Marciniak, P.J. Schuck, A. Bednarkiewicz, Standardization of methodology of

- light-to-heat conversion efficiency determination for colloidal nanoheaters. *ACS Appl. Mater. Interfaces* **13**(37), 44556–44567 (2021). <https://doi.org/10.1021/ACSAMI.1C12409>
184. Z.L. Lei, B. Guo, 2D material-based optical biosensor: status and prospect. *Adv. Sci.* **9**(4), 2102924 (2021). <https://doi.org/10.1002/ADVS.202102924>
185. X. Chen, Y. Zhao, L. Li, Y. Wang, J. Wang et al., MXene/polymer nanocomposites: preparation, properties, and applications. *Polym. Rev.* **61**(1), 80–115 (2020). <https://doi.org/10.1080/15583724.2020.1729179>
186. M.R. Lukatskaya, S. Kota, Z. Lin, M.Q. Zhao, N. Shpigiel et al., Ultra-high-rate pseudocapacitive energy storage in two-dimensional transition metal carbides. *Nat. Energy* **2**(8), 17105 (2017). <https://doi.org/10.1038/nenergy.2017.105>
187. X. Li, X. Yin, H. Xu, M. Han, M. Li et al., Ultralight MXene-coated, interconnected SiCnws three-dimensional lamellar foams for efficient microwave absorption in the X-band. *ACS Appl. Mater. Interfaces* **10**(40), 34524–34533 (2018). <https://doi.org/10.1021/acsami.8b13658>
188. C. Si, K.H. Jin, J. Zhou, Z. Sun, F. Liu, Large-gap quantum spin hall state in MXenes: D-band topological order in a triangular lattice. *Nano Lett.* **16**(10), 6584–6591 (2016). <https://doi.org/10.1021/acs.nanolett.6b03118>
189. F. Wu, K. Luo, C. Huang, W. Wu, P. Meng et al., Theoretical understanding of magnetic and electronic structures of  $Ti_3C_2$  monolayer and its derivatives. *Solid State Commun.* **222**, 9–13 (2015). <https://doi.org/10.1016/J.SSC.2015.08.023>
190. Y. Yue, B. Wang, N. Miao, C. Jiang, H. Lu et al., Tuning the magnetic properties of  $Zr_2N$  MXene by biaxial strain. *Ceram. Int.* **47**(2), 2367–2373 (2021). <https://doi.org/10.1016/J.CERAMINT.2020.09.079>
191. H. Kumar, N.C. Frey, L. Dong, B. Anasori, Y. Gogotsi et al., Tunable magnetism and transport properties in nitride MXenes. *ACS Nano* **11**(8), 7648–7655 (2017). <https://doi.org/10.1021/ACS.NANO.7B02578>
192. J. He, P. Lyu, L.Z. Sun, Á.M. García, P. Nachtigall, High temperature spin-polarized semiconductivity with zero magnetization in two-dimensional Janus MXenes. *J. Mater. Chem. C* **4**(27), 6500–6509 (2016). <https://doi.org/10.1039/c6tc01287f>
193. Y. Lu, X. Qu, S. Wang, Y. Zhao, Y. Ren et al., Ultradurable, freeze-resistant, and healable MXene-based ionic gels for multi-functional electronic skin. *Nano Res.* (2021). <https://doi.org/10.1007/S12274-021-4032-5>
194. K. Allen-Perry, W. Straka, D. Keith, S. Han, L. Reynolds et al., Tuning the magnetic properties of two-dimensional MXenes by chemical etching. *Materials* **14**(3), 694 (2021). <https://doi.org/10.3390/MA14030694>
195. O. Mashtalir, M. Naguib, V.N. Mochalin, Y. Dall’Agnese, M. Heon et al., Intercalation and delamination of layered carbides and carbonitrides. *Nat. Commun.* **4**, 1716 (2013). <https://doi.org/10.1038/ncomms2664>
196. K. Wang, Y. Zhou, W. Xu, D. Huang, Z. Wang et al., Fabrication and thermal stability of two-dimensional carbide  $Ti_3C_2$  nanosheets. *Ceram. Int.* **42**(7), 8419–8424 (2016). <https://doi.org/10.1016/J.CERAMINT.2016.02.059>
197. H. Jing, H. Yeo, B. Lyu, J. Ryou, S. Choi et al., Modulation of the electronic properties of MXene ( $Ti_3C_2T_x$ ) via surface-covalent functionalization with diazonium. *ACS Nano* **15**(1), 1388–1396 (2021). <https://doi.org/10.1021/ACS.NANO.0C08664>
198. V. Shukla, The tunable electric and magnetic properties of 2D MXenes and their potential applications. *Mater. Adv.* **1**(9), 3104–3121 (2020). <https://doi.org/10.1039/D0MA00548G>
199. E.S. Muckley, M. Naguib, I.N. Ivanov, Ultrasensitive, wide-range humidity sensing with  $Ti_3C_2$  film. *Nanoscale* **10**(46), 21689–21695 (2018). <https://doi.org/10.1039/C8NR05170D>
200. T. Hu, H. Zhang, J. Wang, Z. Li, M. Hu et al., Anisotropic electronic conduction in stacked two-dimensional titanium carbide. *Sci. Rep.* **5**, 16329 (2015). <https://doi.org/10.1038/srep16329>
201. Y. Liu, H. Xiao, W.A. Goddard, Schottky-barrier-free contacts with two-dimensional semiconductors by surface-engineered MXenes. *J. Am. Chem. Soc.* **138**(49), 15853–15856 (2016). <https://doi.org/10.1021/jacs.6b10834>
202. C. Si, J. Zhou, Z. Sun, Half-metallic ferromagnetism and surface functionalization-induced metal-insulator transition in graphene-like two-dimensional  $Cr_2C$  crystals. *ACS Appl. Mater. Interfaces* **7**(31), 17510–17515 (2015). <https://doi.org/10.1021/acsami.5b05401>
203. Q. Wan, S. Li, J.B. Liu, First-principle study of Li-ion storage of functionalized  $Ti_2C$  monolayer with vacancies. *ACS Appl. Mater. Interfaces* **10**(7), 6369–6377 (2018). <https://doi.org/10.1021/ACSAMI.7B18369>
204. K.S. Novoselov, D. Jiang, F. Schedin, T.J. Booth, V.V. Khotkevich et al., Two-dimensional atomic crystals. *PNAS* **102**(30), 10451–10453 (2005). <https://doi.org/10.1073/PNAS.0502848102>
205. T. Hu, M. Hu, B. Gao, W. Li, X. Wang, Screening surface structure of MXenes by high-throughput computation and vibrational spectroscopic confirmation. *J. Phys. Chem. C* **122**(32), 18501–18509 (2018). <https://doi.org/10.1021/ACS.JPCCC.8B04427>
206. V.M.H. Ng, H. Huang, K. Zhou, P.S. Lee, W. Que et al., Recent progress in layered transition metal carbides and/or nitrides (MXenes) and their composites: synthesis and applications. *J. Mater. Chem. A* **5**(7), 3039–3068 (2017). <https://doi.org/10.1039/c6ta06772g>
207. M. Naguib, O. Mashtalir, J. Carle, V. Presser, J. Lu et al., Two-dimensional transition metal carbides. *ACS Nano* **6**(2), 1322–1331 (2012). <https://doi.org/10.1021/NN204153H>
208. M. Naguib, J. Come, B. Dyatkin, V. Presser, P.L. Taberna et al., MXene: a promising transition metal carbide anode for lithium-ion batteries. *Electrochem. commun.* **16**(1), 61–64 (2012). <https://doi.org/10.1016/J.ELECOM.2012.01.002>
209. H. Wang, J. Sun, L. Lu, X. Yang, J. Xia et al., Competitive electrochemical aptasensor based on a CDNA-ferrocene/MXene probe for detection of breast cancer marker mucin1. *Anal. Chim. Acta* **1094**, 18–25 (2020). <https://doi.org/10.1016/j.aca.2019.10.003>
210. B. Qiao, Q. Guo, J. Jiang, Y. Qi, H. Zhang et al., An electrochemiluminescent aptasensor for amplified detection of



- exosomes from breast tumor cells (MCF-7 cells) based on G-quadruplex/hemin DNAzymes. *Analyst* **144**(11), 3668–3675 (2019). <https://doi.org/10.1039/C9AN00181F>
211. H. Zhang, Z. Wang, F. Wang, Y. Zhang, H. Wang et al., Ti<sub>3</sub>C<sub>2</sub> MXene mediated Prussian blue in situ hybridization and electrochemical signal amplification for the detection of exosomes. *Talanta* **224**, 121879 (2021). <https://doi.org/10.1016/j.talanta.2020.121879>
212. S. Zhou, C. Gu, Z. Li, L. Yang, L. He et al., Ti<sub>3</sub>C<sub>2</sub>T<sub>x</sub> MXene and polyoxometalate nanohybrid embedded with polypyrrole: ultra-sensitive platform for the detection of osteopontin. *Appl. Surf. Sci.* **498**, 143889 (2019). <https://doi.org/10.1016/J.APSUSC.2019.143889>
213. N. Kurra, B. Ahmed, Y. Gogotsi, H.N. Alshareef, MXene-on-paper coplanar microsupercapacitors. *Adv. Energy Mater.* **6**(24), 1601372 (2016). <https://doi.org/10.1002/aenm.201601372>
214. X. Zhan, C. Si, J. Zhou, Z. Sun, MXene and MXene-based composites: synthesis, properties and environment-related applications. *Nanoscale Horiz.* **5**(2), 235–258 (2020). <https://doi.org/10.1039/C9NH00571D>
215. Y.Y. Peng, B. Akuzum, N. Kurra, M.Q. Zhao, M. Alhabeb et al., All-MXene (2D titanium carbide) solid-state microsupercapacitors for on-chip energy storage. *Energy Environ. Sci.* **9**(9), 2847–2854 (2016). <https://doi.org/10.1039/c6ee01717g>
216. Y. Wang, J. Luo, J. Liu, S. Sun, Y. Xiong et al., Label-free microfluidic paper-based electrochemical aptasensor for ultrasensitive and simultaneous multiplexed detection of cancer biomarkers. *Biosens. Bioelectron.* **136**, 84–90 (2019). <https://doi.org/10.1016/j.bios.2019.04.032>
217. X. Yang, M. Feng, J. Xia, F. Zhang, Z. Wang, An electrochemical biosensor based on AuNPs/Ti<sub>3</sub>C<sub>2</sub> MXene three-dimensional nanocomposite for microRNA-155 detection by exonuclease III-aided cascade target recycling. *J. Electroanal. Chem.* **878**, 114669 (2020). <https://doi.org/10.1016/J.JELECHEM.2020.114669>
218. H. Zhang, Z. Wang, Q. Zhang, F. Wang, Y. Liu, Ti<sub>3</sub>C<sub>2</sub> MXenes nanosheets catalyzed highly efficient electrogenerated chemiluminescence biosensor for the detection of exosomes. *Biosens. Bioelectron.* **124–125**, 184–190 (2019). <https://doi.org/10.1016/J.BIOS.2018.10.016>
219. J. Zhao, C. He, W. Wu, H. Yang, J. Dong et al., MXene-MoS<sub>2</sub> heterostructure collaborated with catalyzed hairpin assembly for label-free electrochemical detection of microRNA-21. *Talanta* **237**, 122927 (2022). <https://doi.org/10.1016/J.TALANTA.2021.122927>
220. F. Vajhadin, M. Mazloum-Ardakani, M. Shahidi, S.M. Moshtaghoun, F. Haghirsadat et al., MXene-based cytosensor for the detection of HER2-positive cancer cells using CoFe<sub>2</sub>O<sub>4</sub>@Ag magnetic nanohybrids conjugated to the HB5 aptamer. *Biosens. Bioelectron.* **195**, 113626 (2022). <https://doi.org/10.1016/J.BIOS.2021.113626>
221. Y. Liu, S. Huang, J. Li, M. Wang, C. Wang et al., 0D/2D heteronanostructure-integrated bimetallic CoCu-ZIF nanosheets and MXene-derived carbon dots for impedimetric cytosensing of melanoma B16–F10 cells. *Microchim. Acta* **188**(3), 69 (2021). <https://doi.org/10.1007/S00604-021-04726-Z>
222. M.A. Sadique, S. Yadav, P. Ranjan, M.A. Khan, A. Kumar et al., Rapid detection of SARS-CoV-2 using graphene-based IoT integrated advanced electrochemical biosensor. *Mater. Lett.* **305**, 130824 (2021). <https://doi.org/10.1016/j.matlet.2021.130824>
223. P. Ranjan, A. Singhal, M.A. Sadique, S. Yadav, A. Parihar et al., Scope of biosensors, commercial aspects, and miniaturized devices for point-of-care testing from lab to clinics applications. *Biosensor Based Advanced Cancer Diagnostics* 395–410 (2022). <https://doi.org/10.1016/B978-0-12-823424-2.00004-1>